

Synthesis, characterization and CMP property of neat and doped mesoporous ceria as defective active particle abrasives



Yang Chen^{a,*}, Pingyang Li^a, Chao Wang^{b,*}, Luning Zhong^a, Ailian Chen^{c,*}

^a School of Materials Science and Engineering, Changzhou University, Changzhou, Jiangsu, 213164, PR China

^b Institute of Machinery Manufacturing Technology, China Academy of Engineering Physics (CAEP), Mianyang, Sichuan, 621900, PR China

^c School of Mechanical Engineering and Rail Transit, Changzhou University, Changzhou, Jiangsu, 213164, PR China

ARTICLE INFO

Keywords:

Mesoporous ceria
Abrasive particle
Chemical mechanical planarization/polishing
Heterogeneous Fenton-like photocatalysis
Persulfate activation

ABSTRACT

A successful chemical mechanical polishing or planarization (CMP) practice generally depends on the physico-chemical properties of abrasive materials, including architecture, morphology, particle size and distribution, surface chemistry, etc. Defect chemistry engineering on CeO₂-based abrasives is fundamentally important to achieve high-performance CMP. Herein, neat and metal (Gd, Y, Zn) doped mesoporous ceria (mCeO₂) particles were synthesized via a modified protective etching strategy. X-ray diffraction, scanning electron microscopy, transmission electron microscopy, nitrogen adsorption-desorption results confirmed the highly uniform particle size and spherical integrity as well as the porous nature of the products. Raman spectroscopy, X-ray photo-electron spectroscopy, ultraviolet-visible diffuse reflectance spectroscopy, scanning transmission electron microscopy-energy dispersive X-ray spectroscopy mapping investigations revealed that the introduction of metal dopants benefited the generation of more Ce³⁺ sites and oxygen vacancy defects, thereby leading to the improved tribocatalytic and photocatalytic activities. Atomic force microscopy results of the polishing tests toward SiO₂ films indicated that the mCeO₂-based abrasives offered highly planarized and scratch-free surfaces with angstrom level roughness, possibly due to their springlike structure and flexible abrasion effects. Especially in the developed mCeO₂-ultraviolet irradiation-potassium persulfate polishing system, the mCeO₂-based abrasives further presented a remarkable improvement in removal efficiency without any loss in surface quality. In this system, the doped mCeO₂ also served as efficient Fenton-like photocatalysts for activating persulfates, producing oxidative reactive-SO₄²⁻ and ·OH radicals and thus promoting the surface modification and material removal. This work provides a valuable reference for developing other functional and effective abrasive systems in reactive oxygen species-facilitated polishing.

1. Introduction

As one of the most significant rare earth oxides, cerium oxide (CeO₂) materials [1–5] with cubic fluorite-type crystallographic symmetry have received widespread interests due to their great potentials for usage in a variety of applications, such as three-way catalysts, photocatalysts, solid-state electrolytes, oxygen storage devices, ultraviolet (UV) blocking materials, polishing abrasives, etc. Chemical mechanical planarization/polishing (CMP) [6–9] appears to be one of most promising technology to remove materials at atomic scale and aims to achieve ultra-smooth and defect-free surfaces. CeO₂-based abrasives originally used for glasses polishing in optic devices for many decades are now applied in integrated circuits manufacture with high CMP performance

toward SiO₂ dielectric films [10–12]. The morphological properties of CeO₂, such as the particle size and distribution, shape, crystallinity, exposed plane, and specific surface area, greatly affect the CMP quality. Various synthetic methods, including hydrothermal crystallization [13, 14], chemical precipitation [15, 16], ionothermal synthesis [17], sol-gel method [18], solvothermal route [19], thermal decomposition [20], supercritical and subcritical dual-stage approach [21], etc., have been developed to prepare CeO₂ particles with tunable dimension.

Many useful properties and applications of CeO₂-based materials are intimately associated with the Ce³⁺/Ce⁴⁺ mixed valences and oxygen vacancy (V_O) defects, which can be nicely adjusted by doping with metallic dopants in CeO₂ lattices. In CMP applications, tailoring the surface chemistry of CeO₂ abrasives has emerged as another important

* Corresponding authors.

E-mail addresses: cy.jpu@126.com (Y. Chen), calcy@cczu.edu.cn (C. Wang), wangchaohit@126.com (A. Chen).

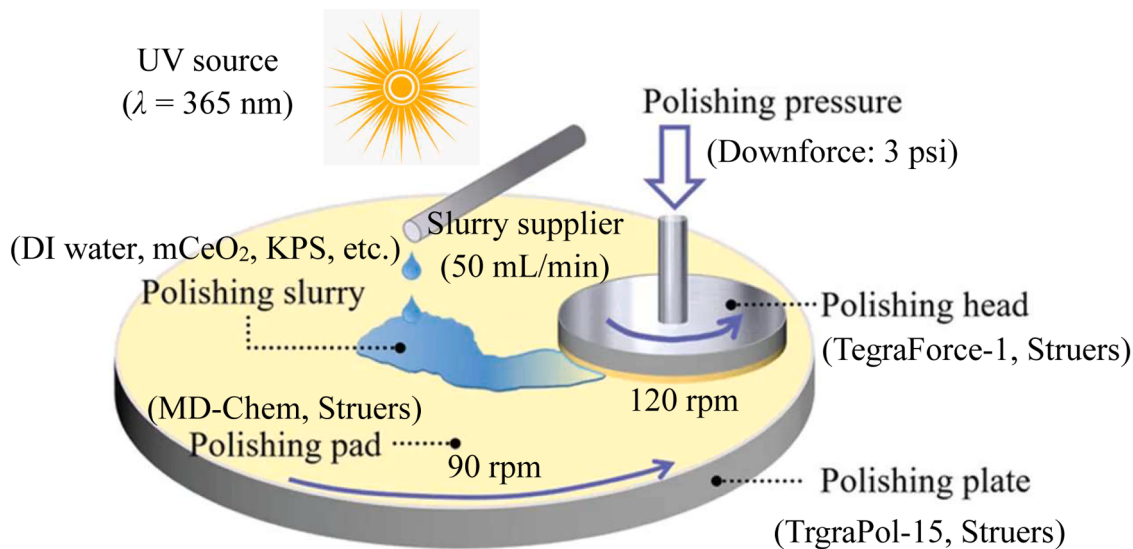


Fig. 1. Schematic illustration of the polishing conditions.

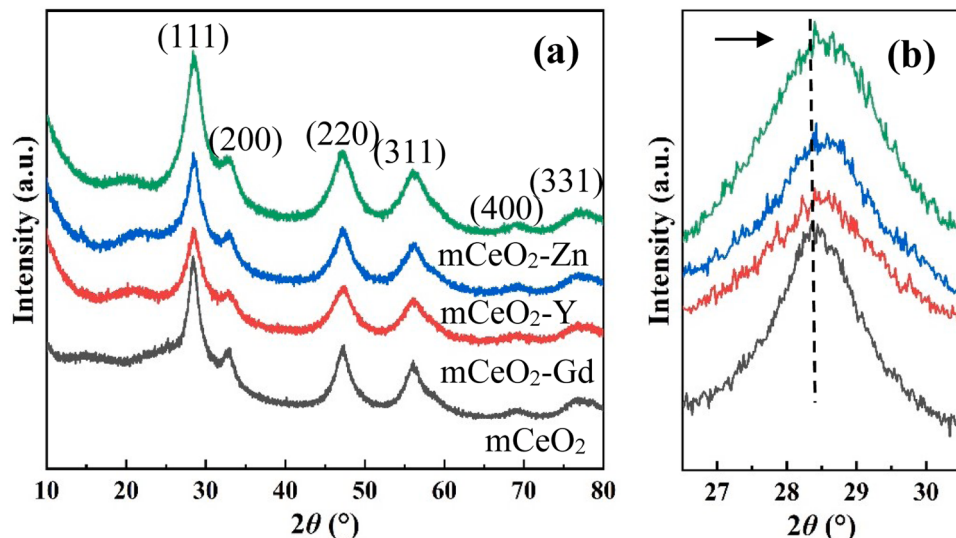


Fig. 2. Wide-angle XRD patterns (a) and amplified patterns in the 2θ range of $26\text{--}31^\circ$ (b) of pure and doped mCeO_2 samples.

aspect as it may lead to further improvements of CMP properties. More and more in-depth studies [22,23] have revealed that the Ce^{3+} and V_0 defects can serve as active sites involved in tribochemical reactions between CeO_2 and SiO_2 , facilitating the formation and breakage of $\text{Ce}-\text{O}-\text{Si}$ bonds and thus accelerating the material removal of CeO_2 toward SiO_2 . As a consequence, impurity doping in CeO_2 abrasives with selective elements is now emerging as an effective strategy for superior CMP activities. Up to now, more attempts have been paid to the optimization of the conventional CMP performance of the doped CeO_2 -involved abrasives [24–33] by incorporation of rare-earth or transition metals, which can availablely control the Ce^{3+} and V_0 concentrations. For further improvement in removal efficiency, doped CeO_2 abrasive systems have been also introduced into photochemical (or

photocatalytic-assisted chemical) mechanical polishing [34–41] based on highly reactive oxygen species (ROS, typically hydroxy radicals $\cdot\text{OH}$) by photocatalytic decomposition of hydrogen peroxide. However, to our knowledge, there are no reports on the ROS-facilitated polishing based on potassium persulfate (KPS) activation using CeO_2 abrasive systems. Compared with $\cdot\text{OH}$ species, many advantages can be expected from the sulfate radicals ($\cdot\text{SO}_4$) produced through persulfate activation, such as longer survival lifetimes (30–40 μs), higher oxidation potentials (2.5–3.1 V), wider working pH range (2.5–11), etc.

The synthesis and optimization of high-quality CeO_2 porous abrasive particles still remain challenging. In this work, the parent and metal (Gd, Y, Zn) doped mesoporous CeO_2 (mCeO_2) particles with uniform sphericity and high monodispersity were prepared using a modified

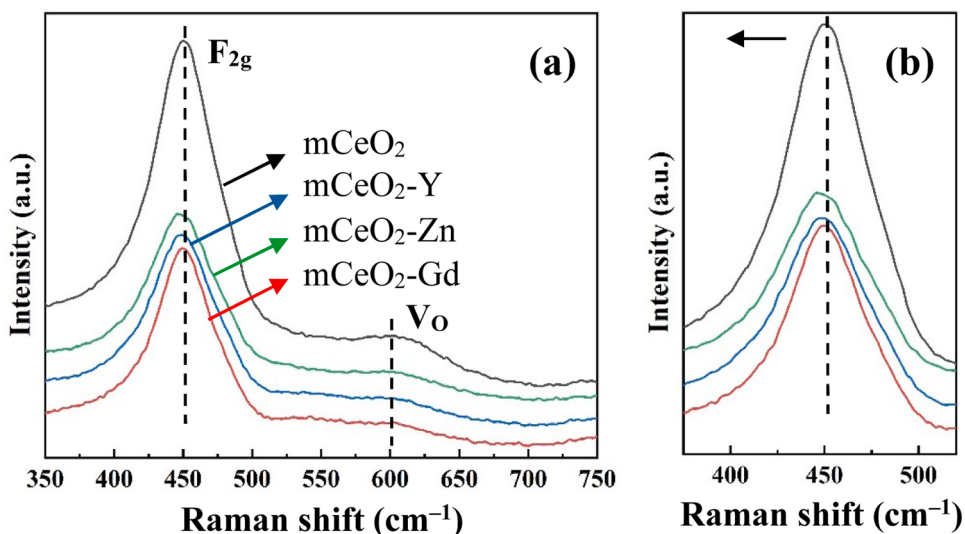


Fig. 3. Raman spectra (a) and amplified profiles of F_{2g} mode (b) of mCeO₂-based samples.

protective etching approach [42]. For doped CeO₂ materials, incorporating lanthanide and transition metal ions can be regarded as a feasible and effective strategy to create surface-defect structures (e.g., Ce³⁺ and V_O). With the metal doping into the CeO₂ lattices, more Ce³⁺ and V_O were generated, which endowed the doped mCeO₂ with enhanced tribochemical and photocatalytic activities. In the as-developed mCeO₂-UV-KPS polishing system (UV-CMP), the doped mCeO₂-based abrasives also served as heterogeneous Fenton-like photocatalysts for KPS activation, and offered an evident improvement in the removal rate without any loss in surface quality. The main advantage of our bottom-up approach to particle synthesis is the predetermined control of the defect chemistry and structure engineering of CeO₂ abrasives.

2. Experimental section

2.1. Materials

Cerium nitrate hexahydrate (Ce(NO₃)₃·6H₂O), gadolinium nitrate hexahydrate (Gd(NO₃)₃·6H₂O), yttrium nitrate hexahydrate (Y(NO₃)₃·6H₂O), zinc acetate dihydrate (Zn(CH₃COO)₂·2H₂O), potassium persulfate (K₂S₂O₈, KPS), ethanol, acetone, sodium hydroxide (NaOH), and polyvinylpyrrolidone (PVP, K30) were all obtained from Sinopharm Group Chemical Reagent Co., Ltd. Ethylene glycol (EG) and hydrochloric acid (HCl, 37%) were obtained from Chinasun Specialty Products Co., Ltd. All chemicals are of analytical grade without further purification. Deionized (DI) water was used throughout the experiments.

2.2. Particle synthesis and characterization

Monodisperse spherical mCeO₂ particles were synthesized by protective etching of PVP-modified oxide precursors with a low amount of inorganic acid according to the previously reported method [42] with some modifications. In a typical procedure, PVP (3.5 g), Ce(NO₃)₃·6H₂O (2.2 g), and EG (20 mL) were charged into a three-necked flask equipped with a magnetic stirrer, a thermometer, and a N₂ inlet. The mixture was heated to 70 °C in an oil bath under magnetic stirring, then heated at 155 °C for 1 h under N₂ protection. After cooling to 120 °C, 0.7 mL of 12 M

HCl was quickly injected into the yellowish slurry to initiate the etching. The process was performed at 120 °C for 1.5 h under N₂ protection and then gradually cooled to room temperature. The resulting products were collected by centrifugation (10,000 rpm), washed with DI water and ethanol several times, and dried at 80 °C. The metal (M: Gd, Y, or Zn) doped mCeO₂ were prepared via a similar procedure, except that a certain amounts of Gd(NO₃)₃·6H₂O, Y(NO₃)₃·6H₂O, or Zn (CH₃COO)₂·2H₂O were also added into the initial reaction system, respectively. In this work, the M/(Ce + M) (M: Gd, Y, or Zn) molar percentage was set at 15%. For brevity, the metal-doped mCeO₂ samples are denoted as mCeO₂-Gd, mCeO₂-Y, and mCeO₂-Zn, respectively.

The crystalline phases of the samples were characterized by X-ray diffraction (XRD) using a Rigaku D/Max 2500 PC diffractometer (Cu K α radiation, $\lambda = 1.5418 \text{ \AA}$, $2\theta = 10\text{--}80^\circ$). The particle morphology and microstructure were examined using a scanning electron microscope (SEM, SUPRA 55, ZEISS). The particle size distribution was obtained using the open-source image processing program Nano Measurer. Transmission electron microscopy (TEM) and high-resolution TEM (HRTEM) images were recorded on a JEOL JEM-2100 electron microscope. High-angle annular dark-field (HAADF) scanning transmission electron microscopy images combined with energy dispersive X-ray spectroscopy (STEM-EDX) maps were acquired using a FEI Talos 200 S electron microscope operated at 300 kV. The surface chemical composition of the prepared samples was examined by X-ray photoelectron spectroscopy (XPS) on a ULVAC- PHI-5000 spectrometer using Al K α radiation (1486.6 eV). The binding energy of the C 1 s peak (BE = 284.8 eV) was used as the reference to calibrate the XPS data. N₂ adsorption-desorption experiments were performed on a Micromeritics TriStar 3020 analyzer at -196 °C to determine the specific surface areas, pore size, and volume of the prepared samples using the Brunauer-Emmett-Teller (BET) method and the Barrett-Joyner-Halenda (BJH) model, respectively. The UV-visible absorption spectra were recorded on an ultraviolet-visible diffuse reflectance spectrometer (UV-Vis DRS, UV-3600, Shimadzu) in the wavelength range from 200 to 800 nm. A ThermoFisher DXR Raman spectrometer at an excitation wavelength of 532 nm was used to collect Raman spectra of the samples.

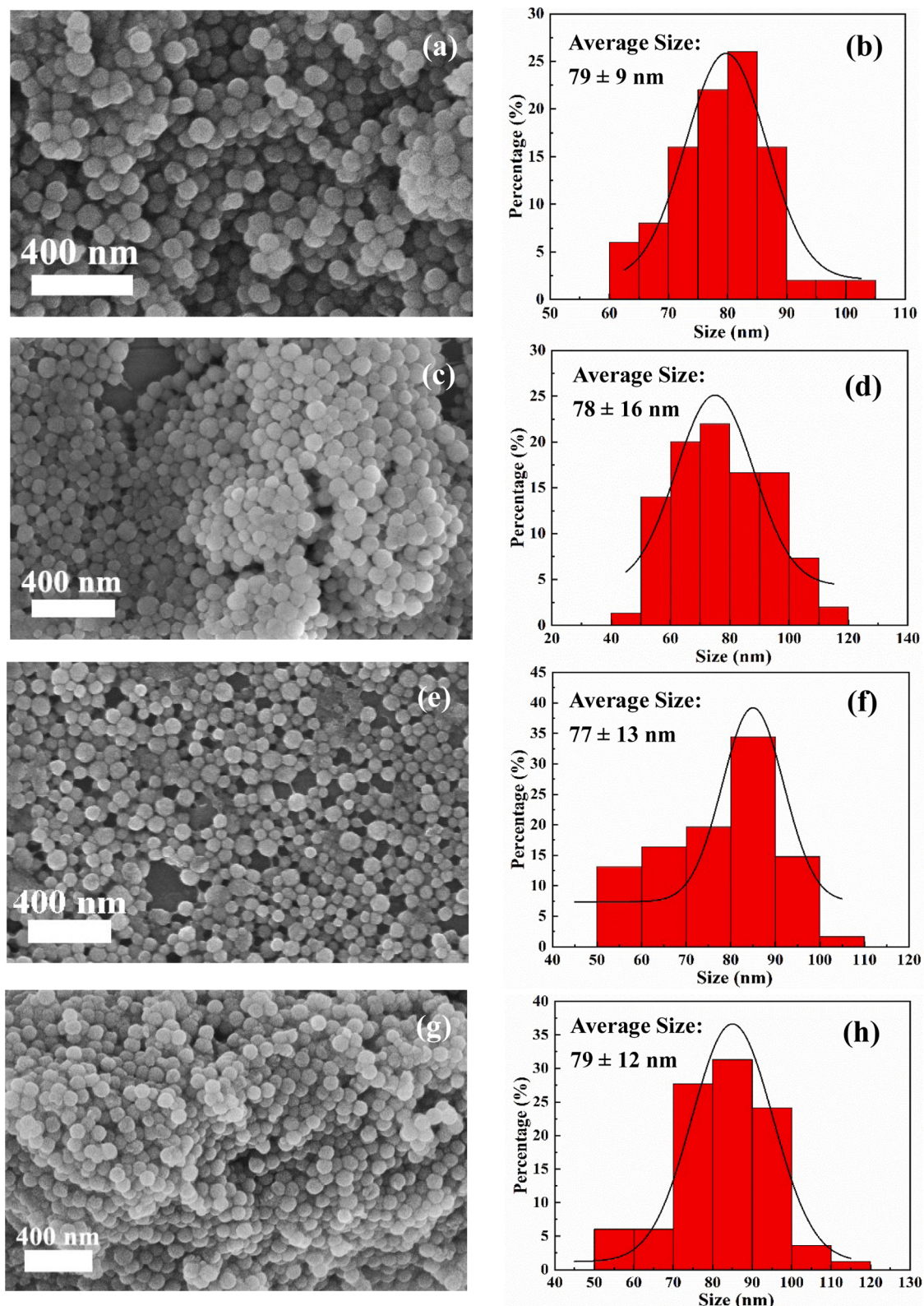


Fig. 4. SEM images and the particle-size distribution histograms of (a, b) mCeO₂, (c, d) mCeO₂-Gd, (e, f) mCeO₂-Y, (g, h) mCeO₂-Zn samples.

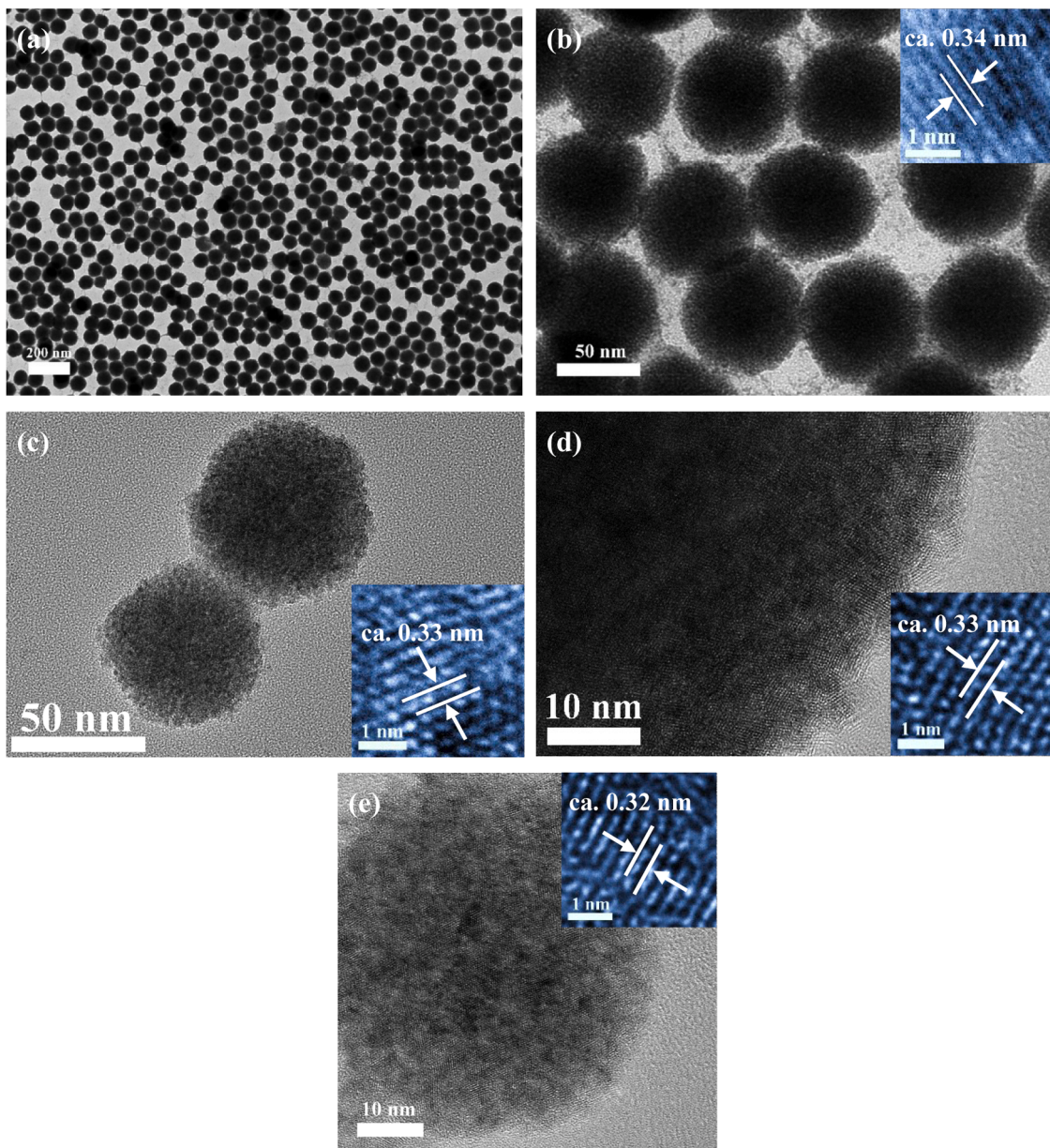


Fig. 5. TEM and HRTEM images of (a, b) mCeO₂, (c) mCeO₂-Gd, (d) mCeO₂-Zn, (e) mCeO₂-Y samples.

2.3. Polishing experiments with mCeO₂ abrasives

Silicon wafers with a 1200 nm thermally grown silicon oxide layer were used as the target materials to be polished and diced into 2.0 cm × 2.0 cm square coupons. Polishing slurries were formulated with one of the mCeO₂-based abrasives at a solid content of 1.0 wt% in DI water. These slurries were then adjusted through pH regulation with 0.1 M NaOH (8.0) and the addition of KPS (5 mM) and PVP surfactants (1.0 wt %). All polishing experiments were carried out on a benchtop polisher (TegraForce-1 & TrgraPol-15 with a porous polyurethane MD-Chem pad, Struers) for 2 min using a slurry supplying rate of 50 mL/min and platen/head speeds of 90/120 rpm at a downforce of 3.0 psi. In UV

irradiation-assisted polishing (UV-CMP), a 250 W halogen lamp ($\lambda = 365$ nm) was installed as a peripheral UV light source. A schematic of the polishing equipment is shown in Fig. 1. After the polishing procedure was over, water polishing was also employed for 30 s using the DI water jet in order to remove the residues from the polished surfaces.

The finished wafers were cleaned by sonication in acetone, rinsed in DI water, and dried in air. Morphology investigations were performed on a Nanoman VS atomic force microscope (AFM, Digital Instruments) & a Dimention V controller with a scan area of $5.0 \times 5.0 \mu\text{m}^2$ and a non-contact 3D optical profilometer (Contour GT, Bruker) with a scan range of $722.1 \times 962.8 \mu\text{m}^2$. AFM topography images and height distributions were recorded in Tapping Mode using Budget Sensors

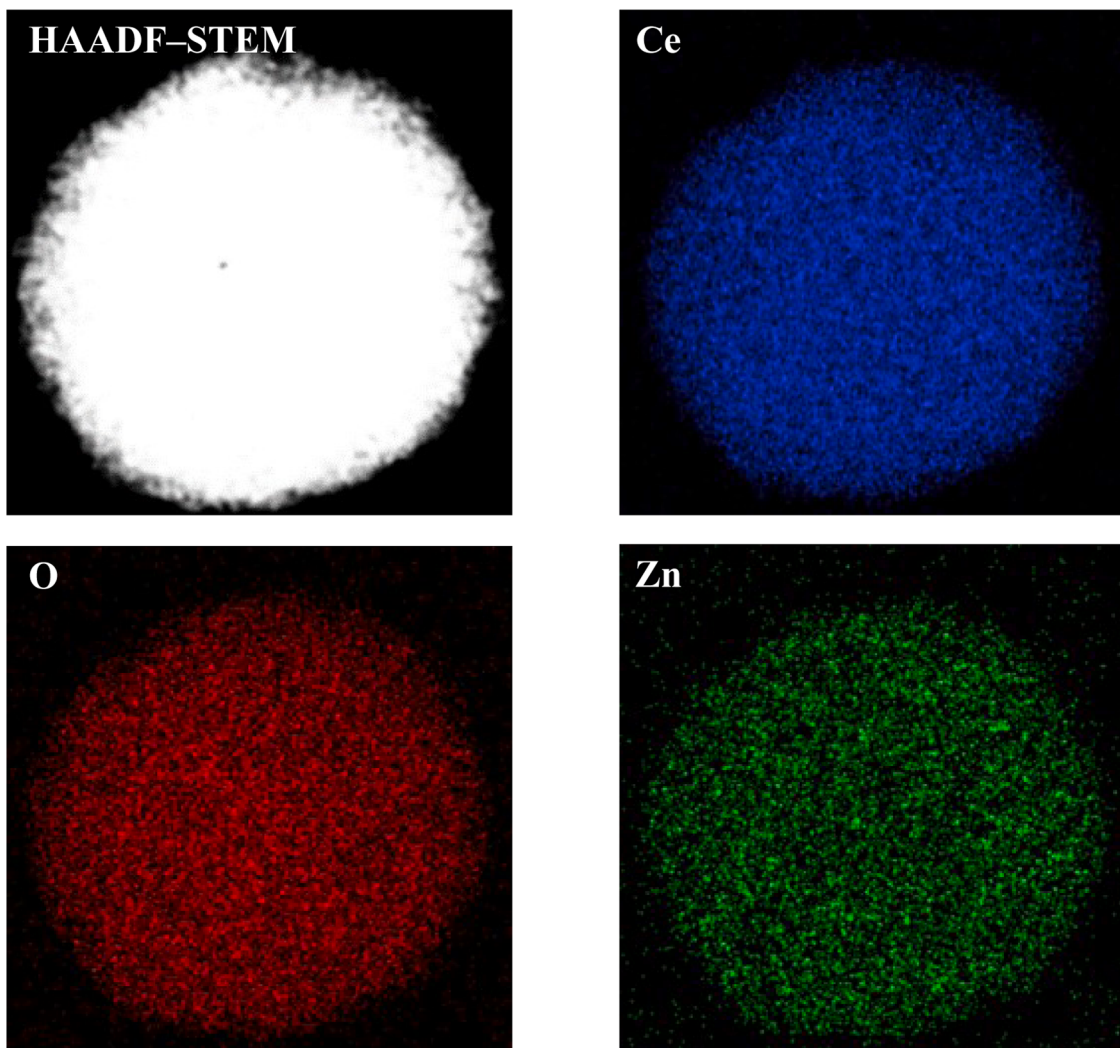


Fig. 6. HADDF-STEM image and EDX elemental maps of an individual $\text{mCeO}_2\text{-Zn}$ particle.

Tap300Al-G probes (< 10 nm of typical tip radius). The weight changes of the substrates before and after polishing were measured using a Mettler Toledo XS105 analytical balance (exact to 0.01 mg). In this work, the material removal rate (*MRR*) was determined using a weight-loss method [34,35]. All the *MRR* and roughness results are the average of three replicated experiments.

3. Results and discussion

3.1. Physical and textural properties of mCeO_2 -based samples

The wide-angle powder XRD patterns of the samples are demonstrated in Fig. 2a. The strong intense diffraction peaks for the pure and doped mCeO_2 materials correspond to JCPDS PDF Card No: 34-0394, and arise from the (111), (200), (220), (311), (400), and (331) crystal planes of the cubic fluorite structure of CeO_2 . No additional diffraction peaks attributed to other metal oxide phases of Gd_2O_3 , Y_2O_3 , or ZnO can be observed from the XRD patterns of the doped samples. Consequently,

the Gd, Y, or Zn species were successfully doped into CeO_2 lattices, thus creating Ce-M-O (M: Gd, Y, Zn) solid solutions rather than metal oxides. As shown in Fig. 2b, the (111) XRD peaks of the doped mCeO_2 samples slightly shift toward a higher 2θ angle side compared to the undoped ones. It may be due to the partial substitution of Ce^{4+} (0.97 Å of ionic radius [42]) sites in CeO_2 lattices by the smaller ionic radii of Gd^{3+} (0.94 Å [43]), Y^{3+} (0.90 Å [44]), or Zn^{2+} (0.74 Å [45]), leading to the lattice contractions and the shift of XRD peaks toward a higher 2θ value. The partial substitution will result in the generation of V_O defects [46,47], which is one of the important characteristics of doped CeO_2 materials, due to the charge compensation and lattice distortion in CeO_2 structures. As expected, the calculated lattice parameter (a) also decreased from 0.5457 nm (mCeO_2) to 0.5408 ($\text{mCeO}_2\text{-Gd}$), 0.5390 ($\text{mCeO}_2\text{-Y}$), and 0.5435 nm ($\text{mCeO}_2\text{-Zn}$). In addition, there is an obvious broadening in the (111) diffraction peaks of the doped mCeO_2 , indicating a decreased grain size in the doped samples. As calculated from the XRD data of the (111) peaks by Scherrer equation, the average crystallite size (d) of mCeO_2 , $\text{mCeO}_2\text{-Gd}$, $\text{mCeO}_2\text{-Y}$, and $\text{mCeO}_2\text{-Zn}$ were determined to be

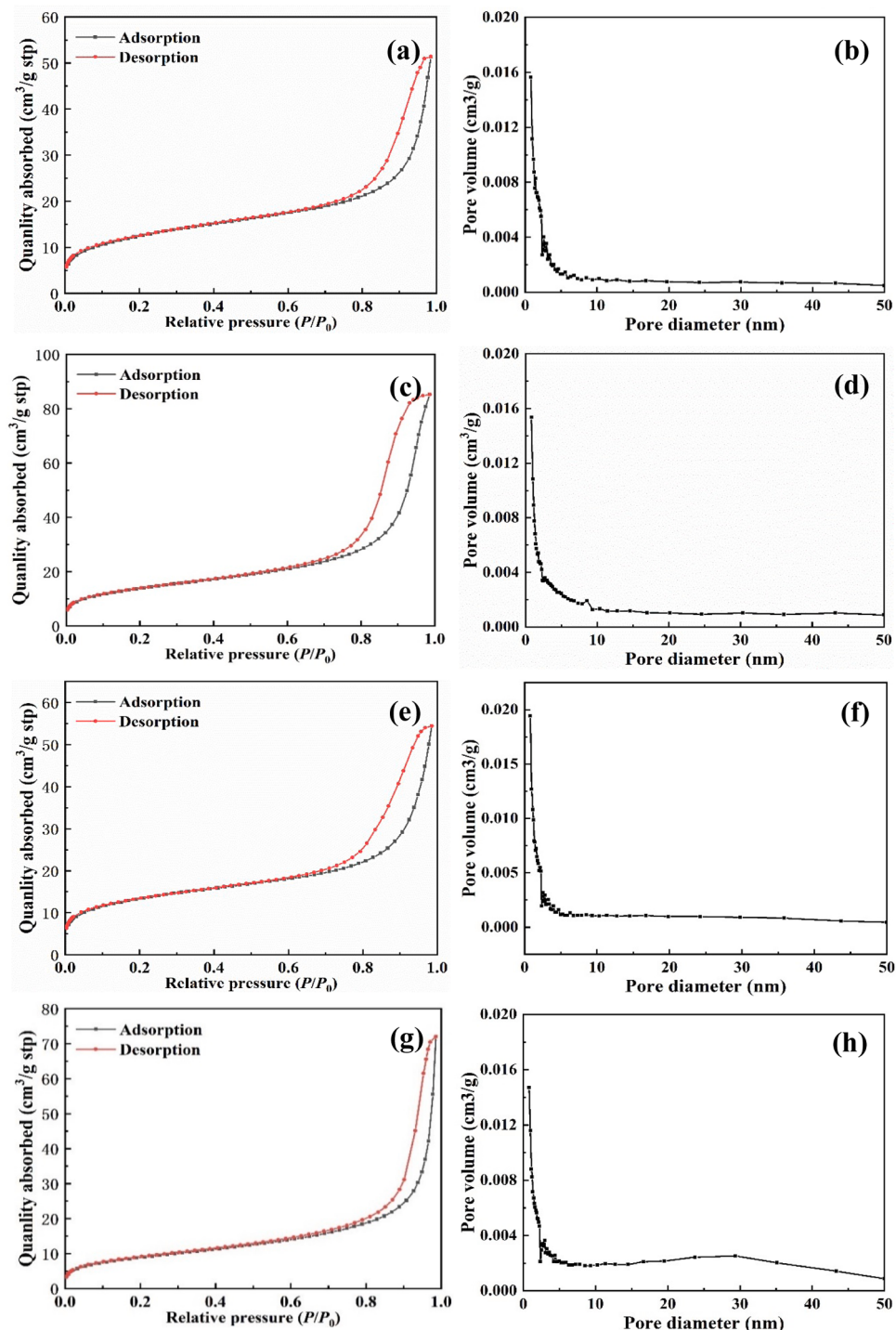


Fig. 7. Nitrogen adsorption–desorption isotherms and pore–size distribution plots of (a, b) mCeO₂, (c, d) mCeO₂-Gd, (e, f) mCeO₂-Y, (g, h) mCeO₂-Zn samples.

Table 1
Physical and textural properties of mCeO₂-based materials.

Samples	α (Å)	d (nm)	S _{A BET} (m ² /g)	D_{pore} (nm)	E_g (eV)	Ce ³⁺ (%)	V _O (%)
mCeO ₂	5.457	10.75	42.02	8.25	2.90	42.98	10.74
mCeO ₂ -Gd	5.408	9.12	47.25	10.08	2.78	48.95	12.23
mCeO ₂ -Y	5.390	9.10	43.69	8.47	2.61	45.59	11.39
mCeO ₂ -Zn	5.435	9.60	50.25	11.24	2.71	45.32	11.33

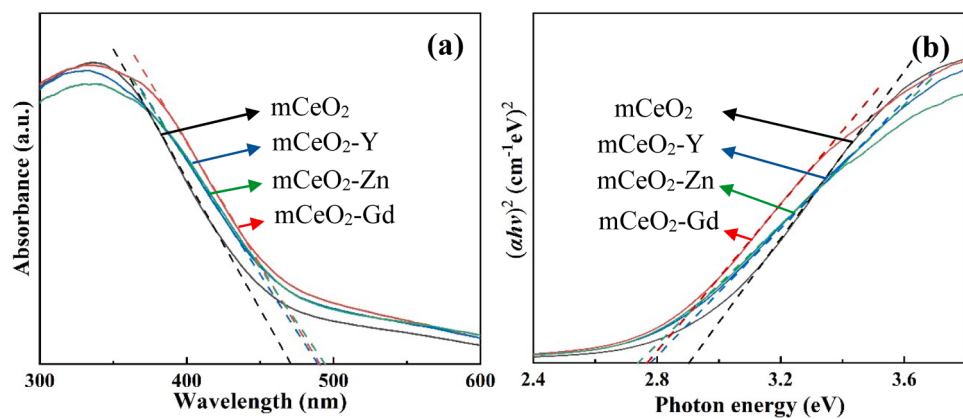


Fig. 8. UV-Vis DRS spectra (a) and the plot of $(\alpha h\nu)^2$ versus photon energy (b) of pure and doped mCeO₂ samples.

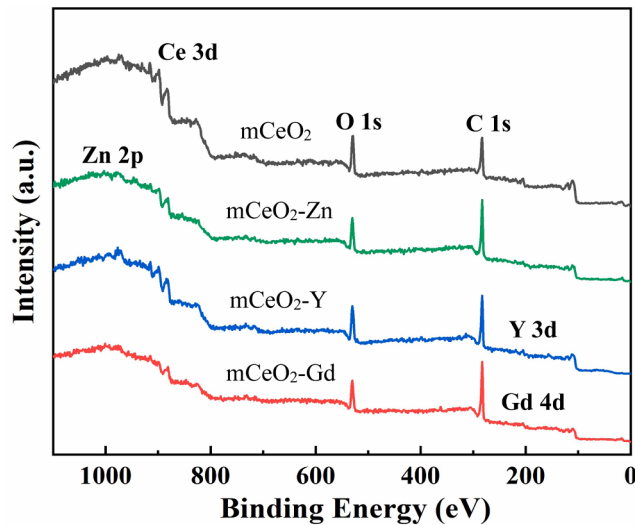


Fig. 9. Wide-range survey XPS spectra of the mCeO₂-based samples.

10.75, 9.12, 9.10, and 9.60 nm, respectively.

Raman spectroscopy is a highly sensitive and effective technique to probe the structure disorder and inherent point defects in CeO₂ materials. Generally, Raman analyzes the existence of V_O defects qualitatively, while XPS prove V_O defects quantitatively [48]. In this work, Raman measurements were performed in order to track the change in V_O defects of pure and mCeO₂ samples. As presented in Fig. 3, the strong Raman signal at 450–460 cm⁻¹ can be ascribed to the F_{2g} vibration mode of the fluorite structure, which is associated with the symmetric stretching mode of the Ce-O₈ vibration unit [49]. Furthermore, the F_{2g} peaks in the Raman spectra of the doped mCeO₂ were slightly blue-shifted by comparison with the pure mCeO₂. It may be attributed to the changes in the bond length of Ce-O, resulted from the incorporation of Gd, Y, or Zn ions into CeO₂ host lattices. Additionally, the much weaker bands located at ca. 600 cm⁻¹ can be assigned to the oxygen defect-induced (D, generally intrinsic V_O defects) mode of CeO₂ [50–52]. The relative intensity ratio of the defect band (I_D) and the F_{2g} band (I_{F2g}) of the CeO₂ fluorite phase, i.e., I_D/I_{F2g} , can be considered as

a good descriptor of the oxygen defects density in CeO₂ materials [53, 54]. It is generally recognized that a higher I_D/I_{F2g} ratio imply more V_O defects in CeO₂ systems [50–54]. Herein, the I_D/I_{F2g} intensity ratio of mCeO₂, mCeO₂-Gd, mCeO₂-Y, and mCeO₂-Zn was found to be 0.1451, 0.1568, 0.1560, and 0.1592, respectively. As revealed by Raman studies, the introduction of Gd, Y, or Zn species into the host mCeO₂ induces an increase in the V_O concentrations due to the redistribution of electrons or disorder of atomic-scale structures.

The morphology of the prepared products was examined by SEM observations. The large-area SEM images (Fig. 4a, c, e, g) of the pure and doped mCeO₂ materials indicate good monodispersity and well-defined sphere morphology. The uniformity and stability of abrasive particles are the key indicators for their CMP applications. To further determine the size distribution, the particle-size distribution histograms of four samples were determined by statistical counting 50 nanospheres in the corresponding SEM images, as shown in Figs. 4b, d, f, h. The average particle size and standard deviation of mCeO₂, mCeO₂-Gd, mCeO₂-Y, mCeO₂-Zn samples were calculated to be 79 ± 8 , 78 ± 16 , 77 ± 13 , and 79 ± 12 nm, respectively. As verified by SEM, the as-prepared mCeO₂-based samples exhibit a comparable particle size and distribution.

The large-area TEM image (Fig. 5a) also confirms the uniformly spherical and monodisperse mCeO₂ particles with diameters of 70–90 nm. The high-magnification TEM images (Figs. 5b–e) further reveal that the mCeO₂-based samples consist of irregular porous structures formed by the disordered stacking of small nanocrystalline domains. For the pure and doped mCeO₂, the corresponding HRTEM images (inset) show the lattice fringes with interplanar distances of 0.32–0.34 nm, corresponding to the (111) planes of cubic phase CeO₂. The slight reduction in lattice spacing can be ascribed to the lattice contraction caused by the partial substitution of Ce⁴⁺ ions with smaller Gd³⁺, Y³⁺, or Zn²⁺ ions.

STEM-EDX spectroscopy is a powerful tool to analyze the chemical composition and element distribution of the samples. Representative HAADF-STEM image and the corresponding STEM-EDX elemental maps of the mCeO₂-Zn are shown in Fig. 6, revealing the coexistence and uniform dispersion of Ce, O, and Zn throughout the individual particle.

Pore properties of the mCeO₂-based samples were characterized by nitrogen adsorption-desorption technique. Fig. 7 shows the adsorption-desorption isotherms and pore-size distribution plots, and the detailed physical and textural parameters of the prepared samples are summarized in Table 1. The physisorption of the pure and doped mCeO₂ presents Type IV isotherms with Type H3 hysteresis loops located in the $P/P_0 = 0.7$ –1.0, inferring the existence of the mesoporous structures with

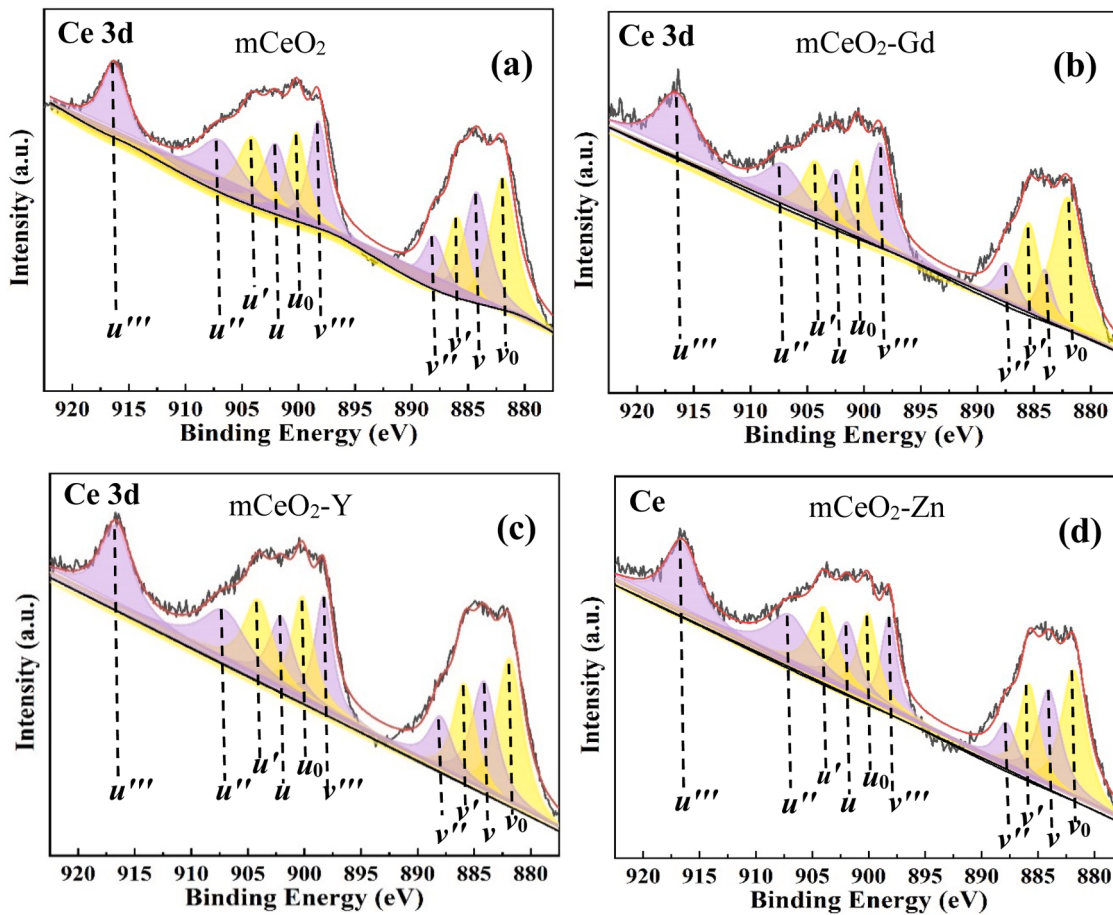


Fig. 10. Ce 3d core level XPS spectra of (a) mCeO₂, (b) mCeO₂-Gd, (c) mCeO₂-Y, (d) mCeO₂-Zn samples.

slit-like pores in frameworks [42]. The BET surface areas (SA_{BET}) of the samples were determined to be 42.02, 47.25, 43.69, and 50.25 m²/g, having corresponding BJH total pore volumes of 0.07, 0.11, 0.08, 0.13 cm³/g and average pore diameters (D_{pore}) centered at 8.25, 10.08, 8.47, 11.24 nm for mCeO₂, mCeO₂-Gd mCeO₂-Y and mCeO₂-Zn, respectively.

UV-Vis diffuse absorbance spectra of the mCeO₂-based samples were collected to investigate their optical absorption properties. As shown in Fig. 8a, all of the samples exhibit the strong ultraviolet absorption in the range of 200–400 nm due to the charge–transfer transition between the O 2p and Ce 4f states in O²⁻ and Ce⁴⁺, which is also the characteristic absorption of CeO₂ materials. By comparison with pure mCeO₂, the metal doped mCeO₂ samples reveal a red shift with a respective relative increase in the absorption range in the visible-light region. It might be attributed to the transformation of Ce⁴⁺ to Ce³⁺ ions and the vacancy faults. The associated optical band-gap energy (E_g) was evaluated based on the absorbance spectra of the samples using the Kubelka-Munk function [55], as shown in Fig. 8b. The optical band gap was determined by extrapolating the straight-line region in the plot of $(\alpha h\nu)^2$ versus photon energy. In this work, the E_g values of mCeO₂, mCeO₂-Gd, mCeO₂-Y, and mCeO₂-Zn were estimated to be 2.87, 2.59, 2.65, 2.74 and 2.79 eV, respectively. A reduction in the optical band gap can be found for the mCeO₂-based samples, as compared with bulk CeO₂ materials (typically ca. 3.2 eV of E_g). Furthermore, the metal doped mCeO₂ exhibit

an improved red shift in the band-gap energy compared with the pristine mCeO₂. It can be attributed to the formation of localized band-gap states (or doping-related transition states) due to the presence of V_O defects and Ce³⁺ions in the doped mCeO₂ skeletons. The narrowed band gap and improved absorption efficiency imply that more photoinduced electron-hole pairs can be generated under light irradiation, which also contribute to an enhanced photocatalysis activity due to the efficiently separated charge carriers and recombination suppression. The band edge positions of the conduction band (E_{CB}) and valence band (E_{VB}) can be further calculated from the following equations [52].

$$E_{VB} = \chi - E_e + 0.5E_g \quad (1)$$

$$E_{CB} = E_{VB} - E_g \quad (2)$$

Herein, χ is the absolute electronegativity of the semiconductor (5.56 eV for CeO₂), E_e is the energy of free electrons on the hydrogen scale (4.5 eV), and E_g is the estimated optical band gap. For the mCeO₂, mCeO₂-Gd, mCeO₂-Y, and mCeO₂-Zn samples, the E_{CB} edge potentials were found to be -0.39, -0.32, -0.33 and -0.30 eV, while the E_{VB} edge potentials were determined to be 2.51, 2.44, 2.45, and 2.42 eV, respectively. These results clearly indicate that incorporating Gd, Y, or Zn dopants into the CeO₂ lattices alter the electronic structures of the metal doping products.

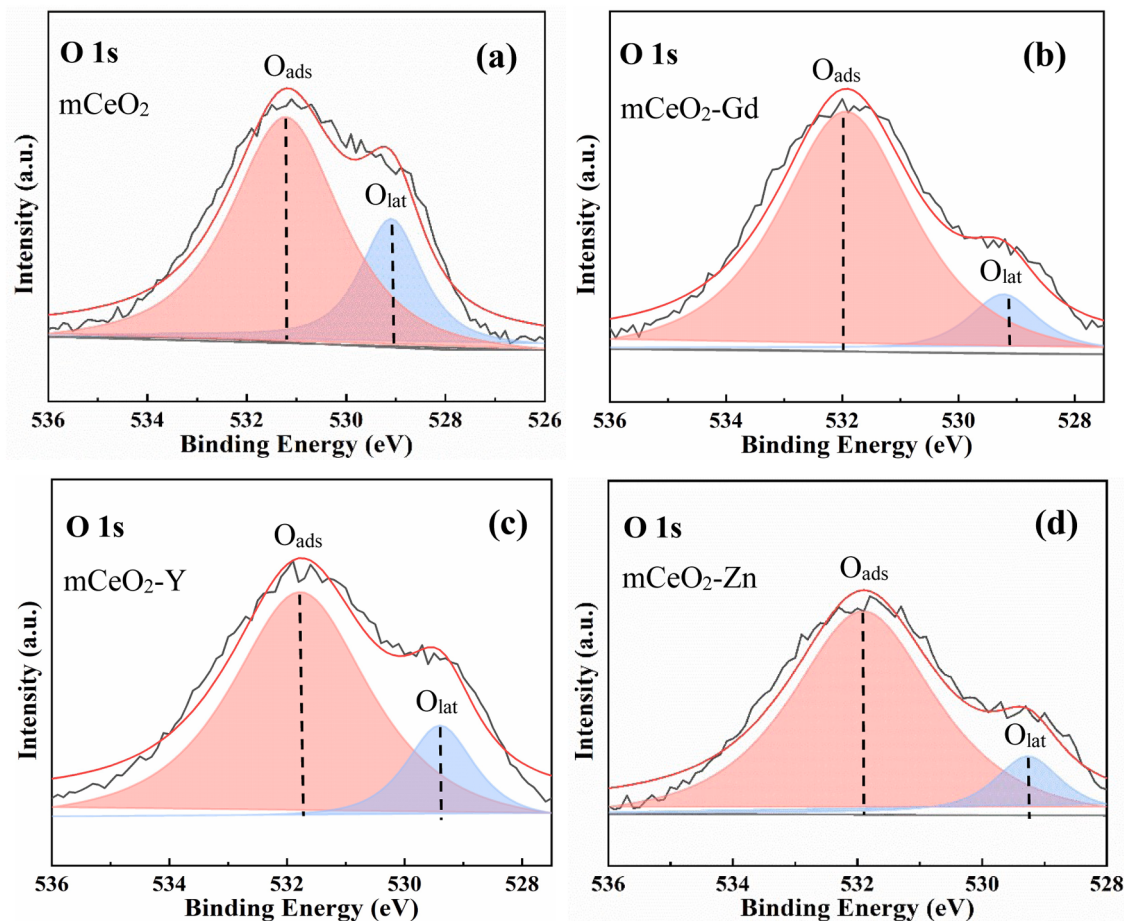


Fig. 11. O 1 s core level XPS spectra of (a) mCeO₂, (b) mCeO₂-Gd, (c) mCeO₂-Y, (d) mCeO₂-Zn samples.

XPS technique was used to illustrate the information of the oxidation state of the elements and surface composition in the prepared samples. For the pure and doped mCeO₂, the existence of Ce, O, or Gd, Y, and Zn elements was identified by the wide-range survey XPS spectra (Fig. 9). Fig. 10 shows the high-resolution Ce 3d core level XPS spectra in the energy range of 875–925 eV and the corresponding Gaussian peak-fitting results of the pure and doped mCeO₂ samples. On account of spin-orbit coupling, the deconvoluted Ce 3d spectra can be resolved into ten binding energy peaks with five pairs of spin-orbit doublets [56]. The peaks denoted as *u* and *v* were attributed to Ce 3d_{3/2} and Ce 3d_{5/2} spin-orbit states, respectively. The labels of (*u*, *v*), (*u'*, *v'*), and (*u''*, *v''*) can be ascribed to Ce⁴⁺ species, associating with the final states of Ce (3d⁹4f⁰) O (2p⁶), Ce (3d⁹4f¹) O (2p⁵) and Ce (3d⁹4f²) O (2p⁴), respectively. The peaks labeled with (*u*₀, *v*₀) and (*u'*, *v'*) can be assigned to Ce³⁺ species, corresponding to the Ce (3d⁹4f¹) O (2p⁶) and Ce (3d⁹4f¹) O (2p⁵), respectively. As shown in Fig. 10, the yellow green peaks are attributed to Ce³⁺, while the purple peaks are assigned to Ce⁴⁺. In addition, the pure and doped mCeO₂ samples have similar binding energy peaks associated with the coexistence of Ce⁴⁺ and Ce³⁺ species. According to the peak areas (*A*), the content of surface Ce³⁺ ions can be calculated using the following Eq. (3). Herein, the order of Ce³⁺ content is as follows: mCeO₂-Gd (48.95%) > mCeO₂-Y (45.59%) > mCeO₂-Zn (45.32%) > mCeO₂ (42.98%), confirming that metal doping

contribute to the enriched Ce³⁺ sites in mCeO₂ materials.

$$\text{Ce}^{3+}\% = \frac{A(\text{Ce}^{3+})}{A(\text{Ce}^{3+}) + A(\text{Ce}^{4+})} = \frac{A_{u_0} + A_{u'} + A_{v_0} + A_{v'}}{(A_{u_0} + A_{u'} + A_{v_0} + A_{v'}) + (A_u + A_{u''} + A_{u'''} + A_v + A_{v''} + A_{v'''})} \quad (3)$$

The Ce³⁺ concentration can also be correlated to the amount of V_O defects. More V_O commonly exist in the CeO₂ systems with higher Ce³⁺ concentrations. Hence, the V_O content of the samples were further estimated by the Eq. (4) [57]. The V_O concentrations were determined to be 10.74%, 12.23%, 11.39%, and 11.33%, for the neat mCeO₂, mCeO₂-Gd, mCeO₂-Y, and mCeO₂-Zn samples, respectively.

$$V_O = 1 - (3 \times \text{Ce}^{3+} + 4 \times \text{Ce}^{4+}) / 4 \quad (4)$$

The surface oxygen species of the mCeO₂-based samples were investigated by the high-resolution O 1 s core level XPS spectra. As shown in Fig. 11, the binding energy peaks at ca. 530.5 and 528.9 eV can be attributed to chemisorbed oxygen species or surface OH⁻ groups (O_{ads}) and lattice oxygen (O_{lat}), respectively. The O_{ads} might be transformed from the active oxygen species adsorbed on O_{lat} through V_O defects [52,58]. According to the integral peak areas, the ratio of the

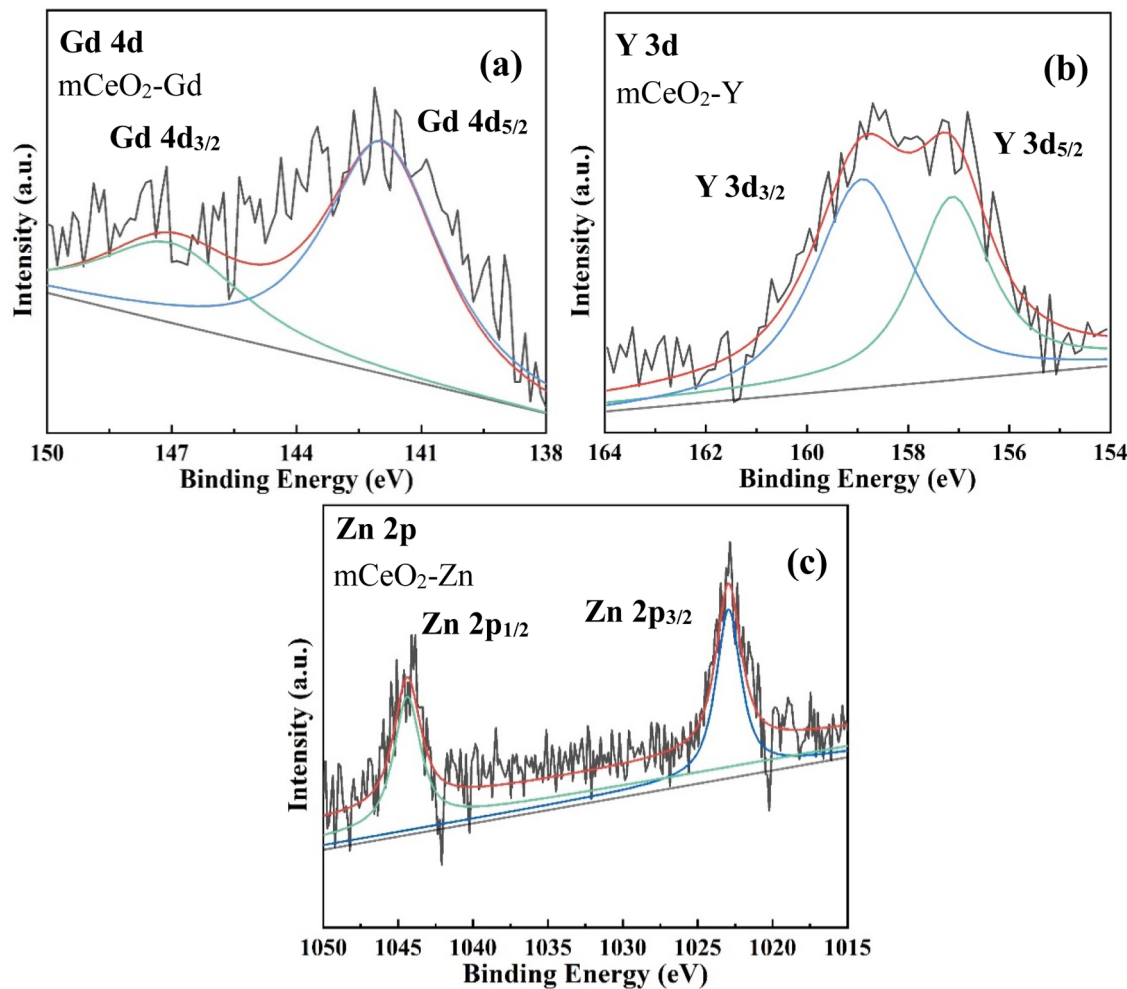


Fig. 12. XPS spectra of (a) Gd 4d, (b) Y 3d, and (c) Zn 2p XPS spectra of the doped mCeO₂ samples.

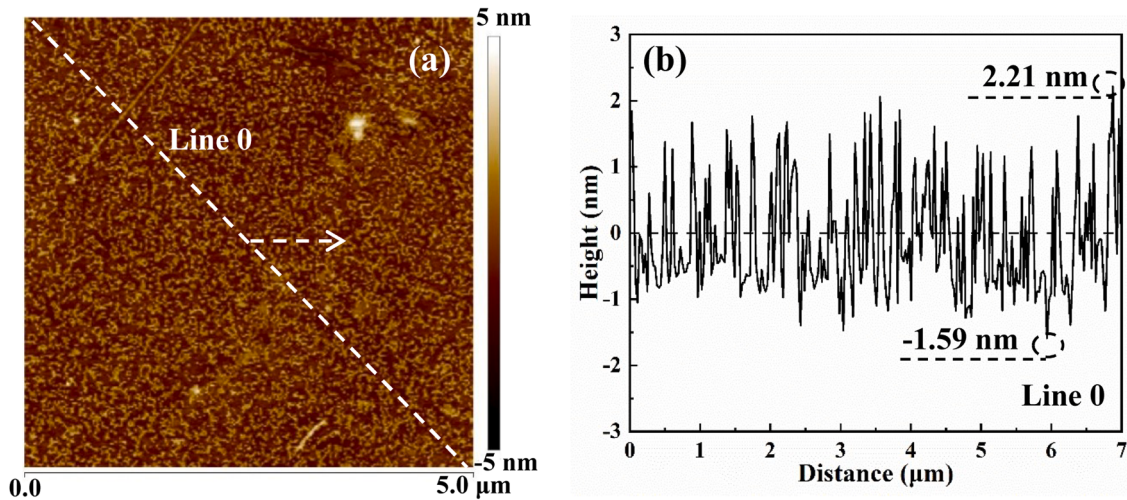


Fig. 13. AFM height image and the line scan profile of the as-received substrate surface.

O_{ads} amount relative to the total oxygen species ($O_{ads}/(O_{ads} + O_{lat})$) increased in the order of mCeO₂ (76.67%) < mCeO₂-Y (83.02%) < mCeO₂-Zn (88.99%) < mCeO₂-Gd (89.32%), indicating that the introduction of the various metals into mCeO₂ endowed the enriched O_{ads} and surface OH⁻ groups in mCeO₂-based materials.

For mCeO₂-Gd samples, the high-resolution Gd 4d spectra (Fig. 12a) revealed the peaks at ca. 141.9 eV (Gd 4d_{5/2}) and 147.1 eV (Gd 4d_{3/2}) assigned to the spin-orbit doublets [59]. As shown in Fig. 12b, the mCeO₂-Y products presented the peaks at 157.3 eV (Y 3d_{5/2}) and 159.5 eV (Y 3d_{3/2}) [60]. In addition, the mCeO₂-Zn samples (Fig. 12c)

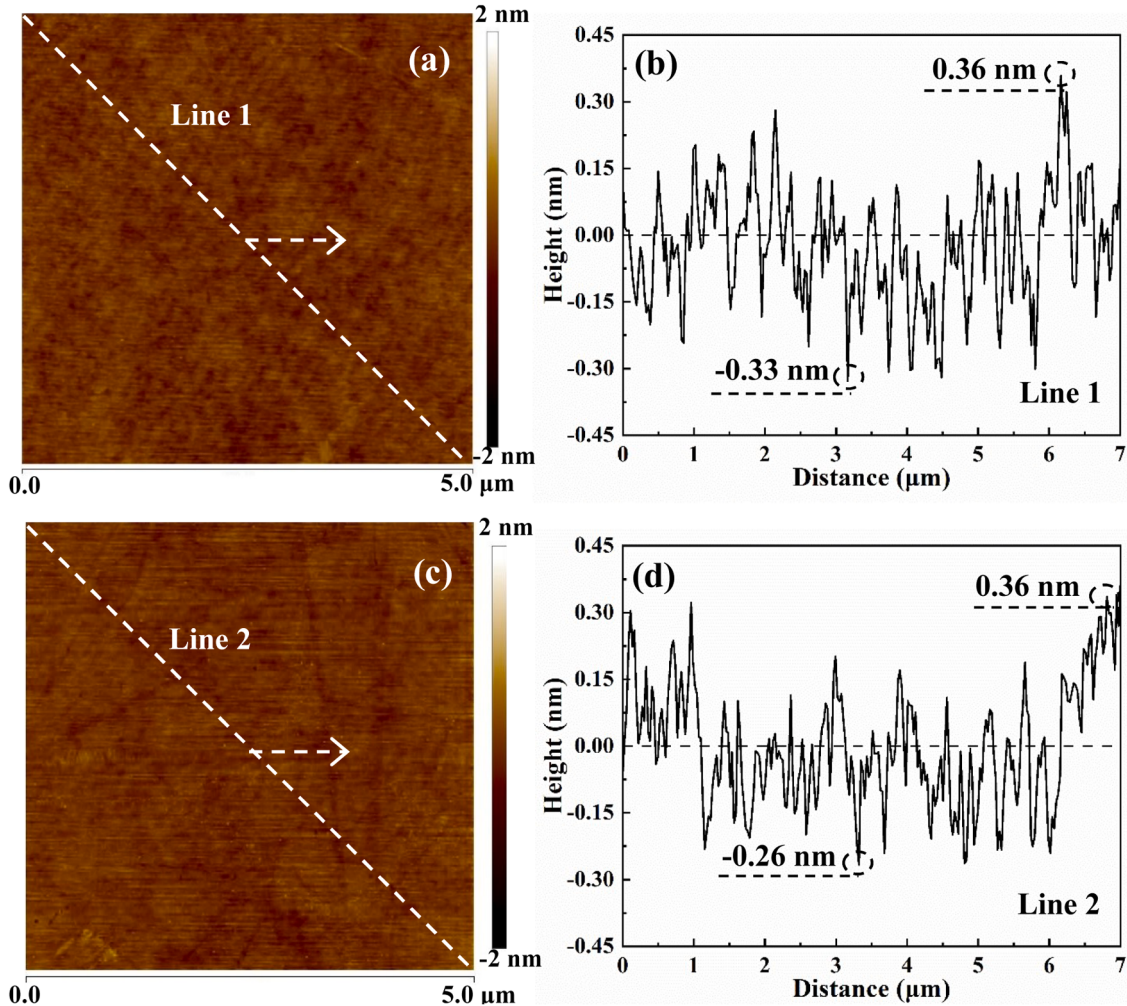


Fig. 14. AFM height image and the line-scan profiles of the substrates after CMP with (a, b) mCeO₂, (c, d) mCeO₂-Zn abrasives.

exhibited the peaks at 1022.7 eV (Zn 2p_{3/2}) and 1044.8 eV (Zn 2p_{1/2}) [61].

3.2. Polishing performance evaluations

Surface quality and removal efficiency are the crucial benchmarks for evaluating the polishing properties of abrasive particles. In this work, the morphology, roughness, and defect of the surfaces before and after polishing were characterized using high-resolution AFM in a scanning range of 5.0 × 5.0 μm². In a two-dimensional (2D) AFM height image, the bright areas indicate the relatively high positions (e.g., peaks), while the dark domains represent the relatively low regions (e.g., valleys). Consequently, more difference in color distribution generally implies a rougher appearance. The typical AFM height image of the as-received wafer clearly confirm this non-uniformity throughout the surface, as shown in Fig. 13a (5.0 nm in Z scale). The arithmetic average roughness (*R_a*) and root-mean-square roughness (*R_q*) were measured to be 7.84 and 9.18 Å, respectively. The line-trace along the white dashed line (Fig. 13b, Line 0) further reveals the topographic variation ranged from +2.21 nm to -1.59 nm, thus determining a peak-to-valley (PV) value of 3.80 nm.

Fig. 14 shows the representative AFM height images (2.0 nm in Z scale) of the substrates after CMP with mCeO₂ and mCeO₂-Zn abrasives, demonstrating the ultra-smooth and scratch-free surfaces. The mean *R_a* and *R_q* roughness of the polished surfaces reduced to 1.25 and 1.59 Å (mCeO₂) as well as 1.18 and 1.81 Å (mCeO₂-Zn), respectively. The topographic variations also decreased to +0.36 ~ -0.33 nm (mCeO₂, PV: 0.69 nm, Line 1) and +0.36 ~ -0.26 nm (mCeO₂-Zn, PV: 0.62 nm, Line 2), respectively. The change in surface topography was also tracked in terms of the corresponding AFM oblique images and lateral views. As shown in Fig. 15, the mCeO₂-based abrasives validly removed the nanoscale asperities from the original wafer, thus creating high-quality surfaces without leaving mechanical scratches or other defects.

The surface characteristics, including AFM height images, profile curvatures, the corresponding oblique images and lateral views (Figs. 16 and 17), also verify the formation of highly planarized wafers after UV-CMP with the neat and doped mCeO₂ abrasives. The topographic variations (Lines 3–6) and PV data were determined to be in the ranges of ±0.4 nm and 0.54–0.70 nm, respectively. To further verify the credibility of the results, the large-scale surface morphology of the wafer after UV-CMP with mCeO₂-Gd abrasives was measured using a 3D optical surface profiler in a scanning range of 722.1 × 962.8 μm². No

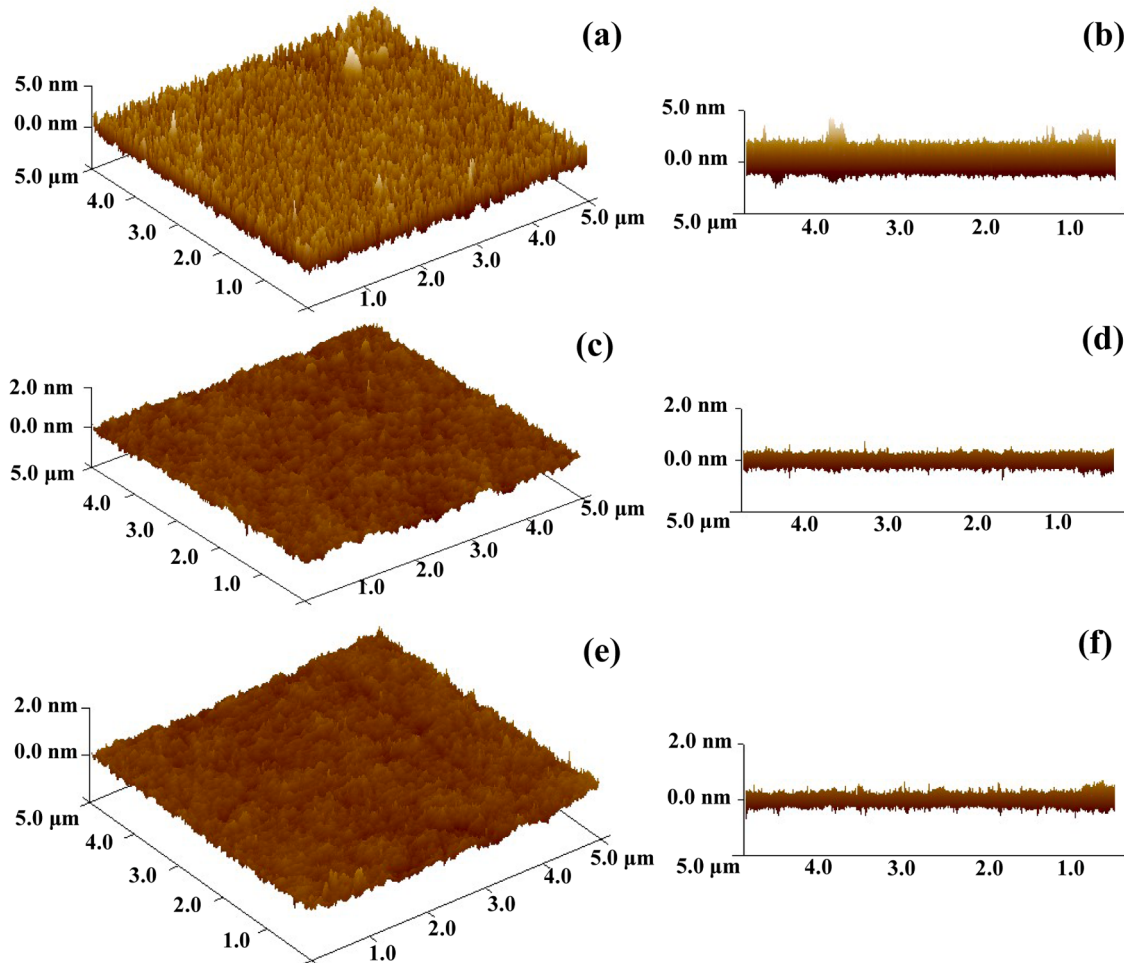


Fig. 15. AFM oblique images and lateral views of the substrates before (a, b) and after CMP with (c, d) mCeO₂, and (e, f) mCeO₂-Zn abrasives.

obvious surface defects such as mechanical scratches, chemical pits, and particle residues can be found from Fig. 18.

Table 2 summarizes the mean R_a and R_q data of the wafers after CMP and UV-CMP experiments. All the mCeO₂-based abrasives achieved the ultra-smooth surfaces with angstrom-level accuracy (typically 1–2 Å of R_q). The pure mCeO₂ abrasives offered a comparable roughness under both CMP (1.59 ± 0.16 Å of R_q) and UV-CMP (1.57 ± 0.12 Å of R_q) conditions. For the metal doped mCeO₂ systems, the surface quality achieved under UV-CMP (1.48–1.76 Å of R_q) is better than those of CMP tests (1.81–2.28 Å of R_q).

The surface quality of the finished wafer highly depends on the processing parameters, pad conditions, component and chemistry of the slurry, physicochemical properties of the abrasive particles, etc. Among these factors, tailoring the mechanical characteristics of abrasive particles is important for the optimization of abrasive-wafer contact behavior and the reduction or even elimination in scratch defects. Fig. 19 shows the schematic illustration of the proposed interface contact between the mCeO₂ abrasives and the polished substrate. In this work, the results of physisorption and TEM clearly confirmed the porous nature of the prepared materials, which could be expected to reduce the overall modulus and hardness of mCeO₂-based particles. The flexible or soft abrasives may elastically deform under an applied downforce,

which generally results in a low friction at the interface and helps to reduce surface damages [62–65]. Therefore, the eliminations in surface damages and scratches can be attributed to the reduced mechanical action during the soft abrasion or soft polishing effects. In addition, the uniform sphericity and high monodispersity of the mCeO₂-based abrasives are beneficial to the further improvement in surface quality [66].

Removal efficiency is another crucial metric for assessing the polishing properties of abrasive particles. In this work, the average MRR data of the pure and metal doped mCeO₂ abrasives are provided in Fig. 20. It can be clearly referred that: (1) MRR s can be effectively enhanced under UV-CMP conditions for all mCeO₂-based abrasives, (2) metal doped mCeO₂ abrasives offer a higher MRR than those pure mCeO₂ in both CMP and UV-CMP experiments. The doped mCeO₂ abrasives offered average MRR s of 105–117 nm/min (UV-CMP), revealing a 26–40% increment compared with pure ones.

In the case of silica polishing with CeO₂ abrasives, the effective material removal can be well interpreted from the classical chemical-tooth mechanism, as proposed by Cook [67]. In this model, the SiO₂ surface reacted with H₂O molecules or OH[−] groups in slurries, thus generating a soft hydroxylated layer of Si(OH)₄. Meanwhile, the surface of CeO₂ was also dissociated by H₂O to form Ce-OH bonds. The silicates could be adsorbed to CeO₂ surfaces through the interaction with

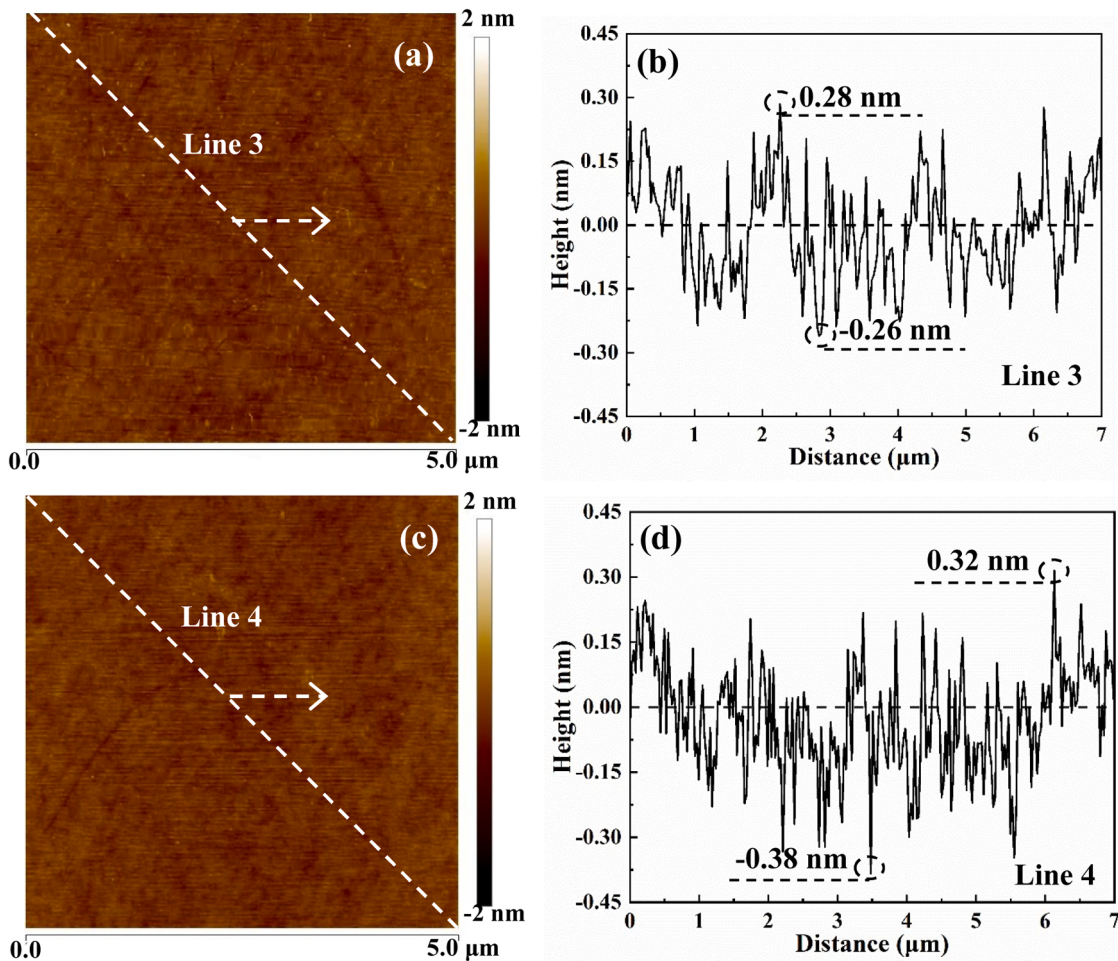


Fig. 16. AFM height images and the line-scan profiles of the wafers after UV-CMP with (a, b) mCeO₂, (c, d) mCeO₂-Gd, (e, f) mCeO₂-Y, (g, h) mCeO₂-Zn abrasives.

—OH groups [68]. The Ce—OH structures would react with the hydroxylated layer to form Si—O—Ce bonds, which exhibited a higher bonding energy than Si—O—Si bonds [69,70]. Moreover, the applied mechanical force might contribute to promoting the formation of Ce—O—Si structures. With the assistance of shear force and relative sliding, the interfacial Si atoms could be efficiently removed from SiO₂ surfaces through the multiple dynamic formation and breakage of Ce—O—Si bonds. These processes can be described in the following Eqs. (5)–(10).



Surface chemistry of abrasive particles also plays a crucial role in CMP practices. In-depth studies clearly confirm that there is a reliable correlation between the material removal rates in oxide-CMP and

surface-defect structures of CeO₂ abrasives. In particular, the Ce³⁺ and V_O defects can be regarded as the tribocchemically active sites, prominently promoting the formation and breakage of Ce—O—Si bonds at CeO₂—SiO₂ interfaces [22,23] and thus facilitating the material removal of CeO₂ towards SiO₂. In this work, the results of XPS, Raman, and UV-Vis DRS confirmed that the metal (Gd, Y, or Zn) doping contributed to creating more Ce³⁺ sites and V_O defects in mCeO₂ materials. Consequently, the doped mCeO₂ abrasives offered a greater tribocchemical activity and higher oxide removal rate than that of the undoped ones.

In UV-CMP, a series of heterogeneous Fenton-like photocatalysis reactions may be involved in surface modification and material removal. A possible mechanism for the production of active species in the CeO₂-UV-KPS polishing system is illustrated in Fig. 21. Under UV-light illumination, the photoinduced electrons (e⁻) in mCeO₂ were excited and immigrated from the VB to the CB, and holes (h⁺) were left in the VB, thus contributing to the separation of photogenerated e⁻—h⁺ pairs [71, 72]. The h⁺ could react with water molecules or OH⁻ to produce ·OH radicals. A portion of photogenerated e⁻ could combine with the dissolved oxygen to form superoxide radicals (·O₂[·]). Another portion of e⁻ could react with S₂O₈²⁻ to generate ·SO₄[·] radicals. The produced ·SO₄[·] could also combine with water molecules or OH⁻ to form ·OH. As

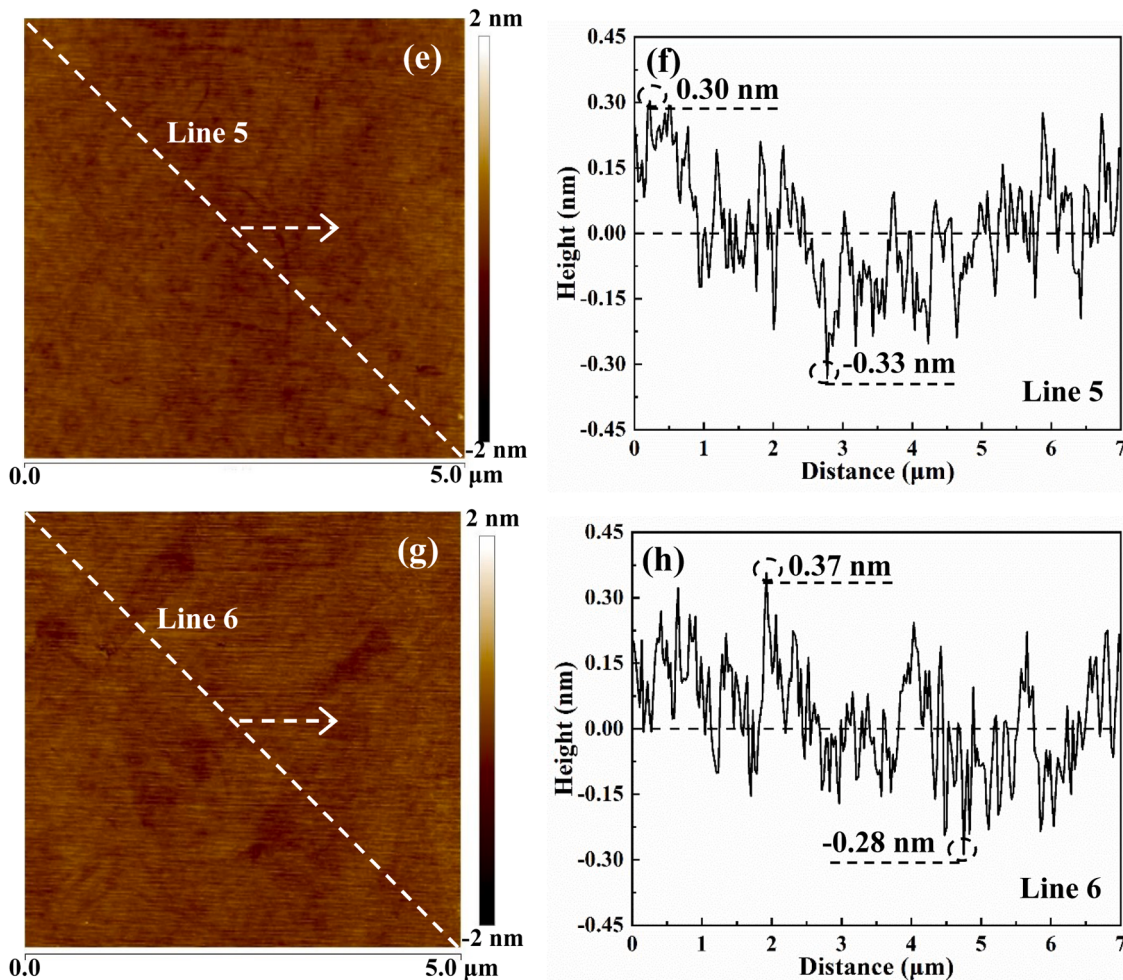
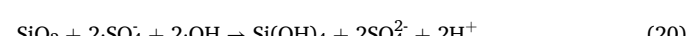
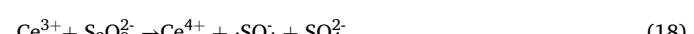
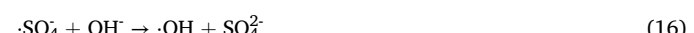


Fig. 16. (continued).

catalytic active sites, the Ce³⁺ at mCeO₂ surfaces would donate electrons for KPS activation [73–75]. Therefore, the Ce³⁺/Ce⁴⁺ couples involved in mCeO₂ could participate in the reduction of S₂O₈²⁻ to produce ·SO₄. Meanwhile, the Ce⁴⁺ species might capture photoinduced e⁻ and converted into Ce³⁺, restricting the recombination of photo-generated charges and thus promoting the electron transfer between Ce³⁺ and Ce⁴⁺[76]. Consequently, the oxidative reactive species including ·OH, ·SO₄, and ·O₂ could coexist in the heterogeneous Fenton-like photocatalysis system. These processes can be briefly described by Eqs. (11)–(18). In UV-CMP, the highly reactive species might directly react with SiO₂ [77–79], thus accelerating the generation of Si(OH)₄ products, as proposed in Eqs. (19) and (20). The separated h⁺ may also participate in the SiO₂ surface modification.



In this study, the reactive species produced from the Fenton-like photocatalysis process can be expected to enhance the surface modification of SiO₂ materials, facilitating the production of chemically reacted products that can be tribochimically and mechanically removed by CeO₂ abrasives. Therefore, the mCeO₂-based abrasives offered a remarkable improvement in the removal efficiency in UV-CMP experiments, as compared with the conventional CMP.

Surface defects of CeO₂-based materials such as Ce³⁺ and V_O generally reduce the band-gap energy and prevent the photo-induced hole-electron recombination [51,80,81]. Due to the presence of enriched Ce³⁺ and V_O defects, the metal doped mCeO₂ materials had sufficient

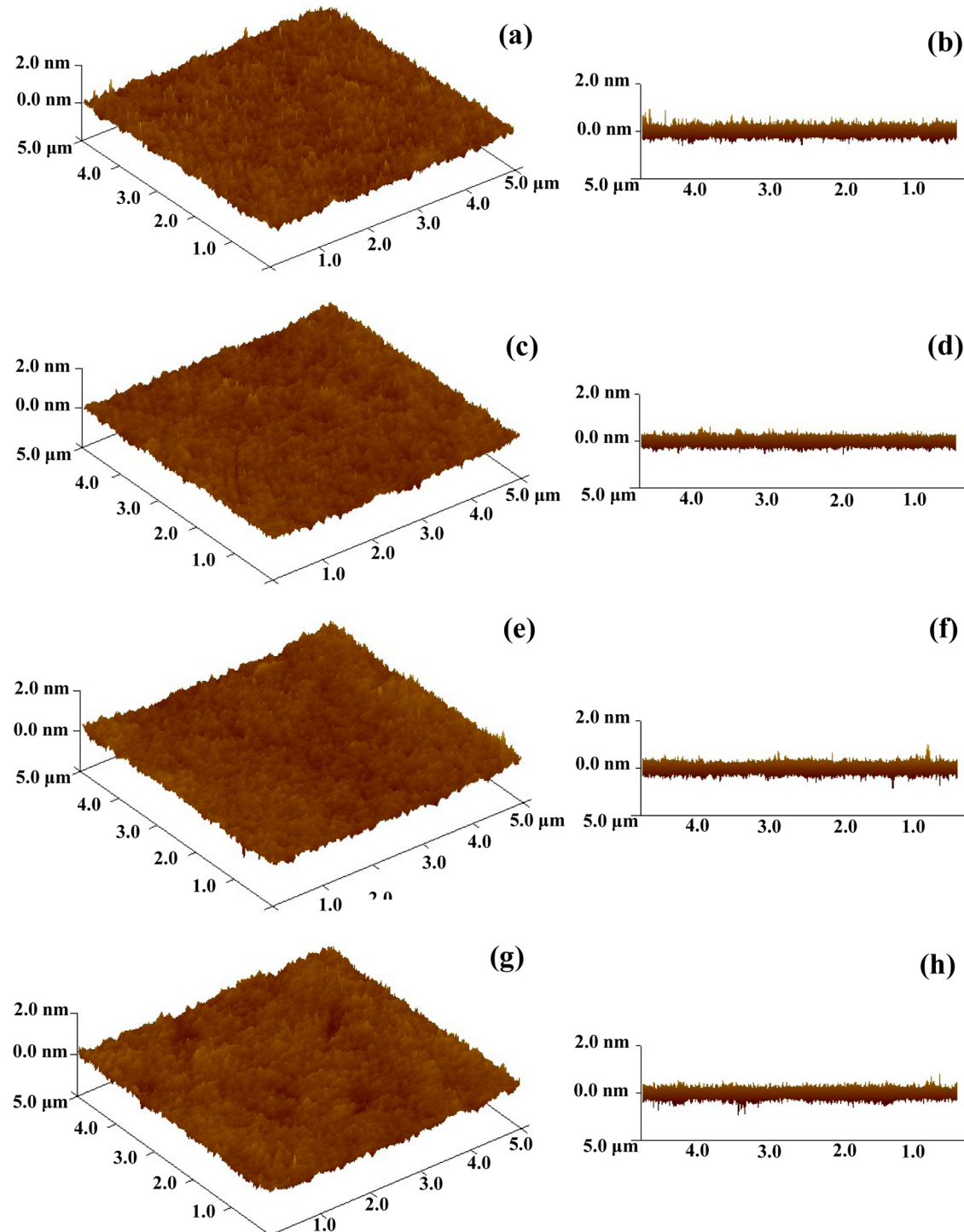


Fig. 17. AFM oblique images and lateral views of the surfaces after UV-CMP with (a, b) mCeO₂, (c, d) mCeO₂-Gd, (e, f) mCeO₂-Y, (g, h) mCeO₂-Zn abrasives.

surface-active sites and improved photocatalytic activity. In addition, the doped Gd, Y, or Zn ions may behavior as e^- -acceptors and/or h^+ donors, also promoting the transfer of e^- and h^+ . Therefore, the mobility and generation of photogenerated carriers can be promoted in the

defective metal-doping mCeO₂, accelerating the separation of photo-induced e^- - h^+ pairs and thus contributing to the production of ·OH and ·SO₄ species. In this study, the doped mCeO₂ abrasives offered a higher removal rate than undoped ones under UV-CMP conditions,

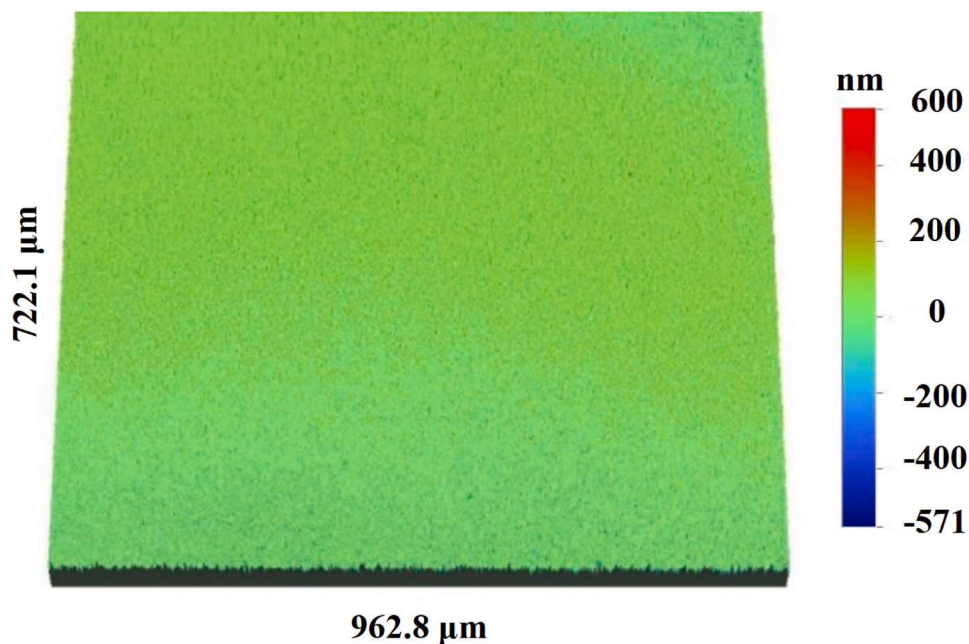


Fig. 18. Non-contact 3D optical morphologies over $772.1 \times 962.8 \mu\text{m}^2$ of the surfaces after UV-CMP with mCeO₂-Gd abrasives.

Table 2

Surface roughness data of the substrates after CMP and UV-CMP with different mCeO₂-based abrasives.

Abrasive types		<i>R_a/R_q (Å)</i>			
		Run 1	Run 2	Run 3	Average
mCeO ₂	CMP	1.21/1.54	1.40/1.77	1.15/1.46	$1.25 \pm 0.13 / 1.59 \pm 0.16$
	UV-CMP	1.25/1.66	1.24/1.61	1.11/1.43	$1.20 \pm 0.08 / 1.57 \pm 0.12$
mCeO ₂ -Gd	CMP	1.14/1.56	1.21/1.92	1.27/2.32	$1.20 \pm 0.07 / 1.93 \pm 0.38$
	UV-CMP	1.13/2.10	1.04/1.35	1.21/1.83	$1.13 \pm 0.09 / 1.76 \pm 0.38$
mCeO ₂ -Y	CMP	1.57/2.12	1.61/2.53	1.58/2.20	$1.59 \pm 0.02 / 2.28 \pm 0.22$
	UV-CMP	1.19/1.51	1.16/1.47	1.17/1.47	$1.17 \pm 0.02 / 1.48 \pm 0.02$
mCeO ₂ -Zn	CMP	1.27/2.32	1.12/1.60	1.14/1.51	$1.18 \pm 0.08 / 1.81 \pm 0.44$
	UV-CMP	1.02/1.30	1.20/1.54	1.25/1.61	$1.16 \pm 0.12 / 1.48 \pm 0.16$

possibly resulting from the improvements in both photocatalytic activity and tribocatalytic reactivity. Herein, we compare the as-prepared neat and doped mCeO₂ abrasives with the previously reported CeO₂-based

ones, and the polishing performances (typically surface roughness and removal rate) towards SiO₂ films are summarized in Table 3. It is reasonable to believe that the appropriate particle size, good uniformity

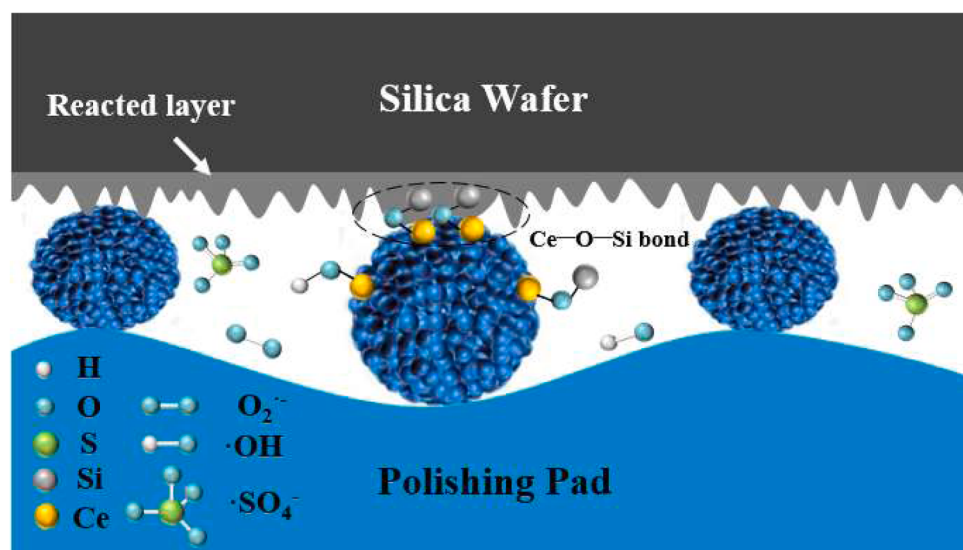


Fig. 19. Schematic illustration of the proposed mCeO₂-substrate interface contact state.

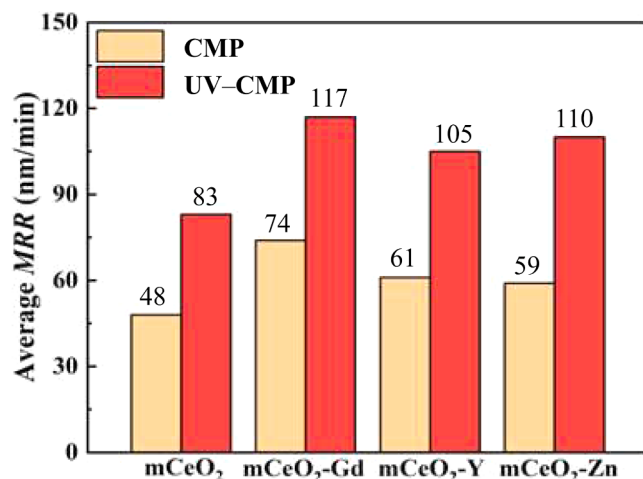


Fig. 20. MRR data of the mCeO_2 -based abrasives.

in morphology and sphericity, porous structure, enhanced elastic response, defective surfaces, enriched Ce^{3+} sites and V_0 defects, narrowed band gap are the essential factors to achieve the superior CMP

and UV-CMP performance of the mCeO_2 -based abrasives.

4. Conclusions

In summary, the neat and metal (Gd, Y, Zn) doped mesoporous ceria (mCeO_2) nanospheres with uniformly distributed sizes were synthesized through a protective etching approach. As confirmed by XPS, Raman, and UV-vis DRS, incorporating metal ions in the mCeO_2 lattices led to the evolution of more Ce^{3+} sites and V_0 defects, which contributed to the enhancement in photocatalytic and tribocatalytic activities. The proposed $\text{CeO}_2\text{-UV-KPS}$ polishing system based on heterogeneous Fenton-like photocatalysis reactions was proven to be effective in improving removal rate towards silica films without any loss in surface quality. Herein, the defective mCeO_2 served as Fenton-like photocatalysts for KPS activation. Benefiting from the porous and flexible mCeO_2 -based abrasives, the elimination in surface scratches should be attributed to the reduced mechanical action or low friction at the abrasive–substrate interface. The enhanced removal efficiency might be assigned to the highly oxidative reactive species ($\text{SO}_4^{\cdot-}$, $\text{OH}^{\cdot-}$, etc.) produced from the Fenton-like reaction and photocatalysis process occurred in the coupling system. The involved surface modification and Fenton-like photocatalysis synergy should be further investigated in terms of In-situ XPS, In-situ Raman, In-situ Fourier-transformed infrared

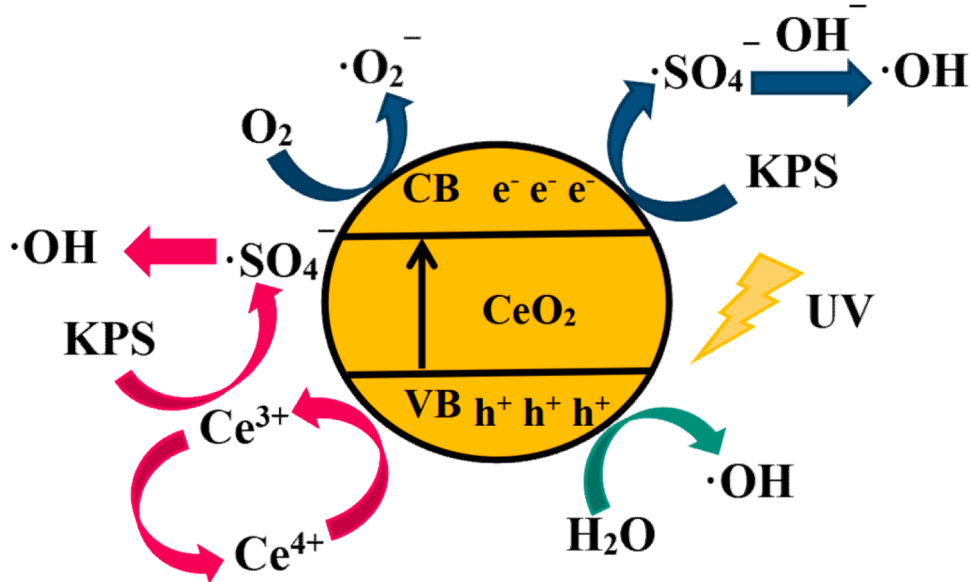


Fig. 21. The possible Fenton-like photocatalysis mechanism for the $\text{mCeO}_2\text{/UV/KPS}$ system.

Table 3

Summary of the polishing performances of CeO_2 -based abrasives towards SiO_2 films.

Abrasive types	Particle size (nm)	Surface roughness (nm, R_a)	Removal rate (nm/min)	Reference
Single-crystal CeO_2	60 ± 12	$0.53 (10.0 \times 10.0 \mu\text{m}^2)$	414	[15]
CeO_2 nanoparticles	39 ± 5	$0.60 (10.0 \times 10.0 \mu\text{m}^2)$	251	[16]
Porous CeO_2	70–90	$0.11 (5.0 \times 5.0 \mu\text{m}^2)$	61	[26]
Porous CeZrO_2	60–80	$0.11 (5.0 \times 5.0 \mu\text{m}^2)$	88	[26]
Porous CeGdO_2	60–80	$0.14 (5.0 \times 5.0 \mu\text{m}^2)$	109	[26]
Porous CeO_2	80–180	$0.30 (3.0 \times 3.0 \mu\text{m}^2)$	81	[31]
Porous $\text{CeO}_2\text{-Nd}$	80–180	$0.54 (3.0 \times 3.0 \mu\text{m}^2)$	126	[31]
mCeO_2	273 ± 19	$0.15 (5.0 \times 5.0 \mu\text{m}^2)$	124	[32]
mCeYbO_2	271 ± 15	$0.13 (5.0 \times 5.0 \mu\text{m}^2)$	185	[32]
pCeO_2	200	$0.29 (5.0 \times 5.0 \mu\text{m}^2)$	252	[33]
La-doped CeO_2	200	$0.20 (5.0 \times 5.0 \mu\text{m}^2)$	338	[33]
Pr-doped CeO_2	200	$0.23 (5.0 \times 5.0 \mu\text{m}^2)$	306	[33]
Nd-doped CeO_2	200	$0.22 (5.0 \times 5.0 \mu\text{m}^2)$	295	[33]
Nd-doped PS/ CeO_2	105	$0.36\text{--}0.46 (2.0 \times 2.0 \mu\text{m}^2)$	66–174	[36]
Neat and doped mCeO_2	80	$0.12\text{--}0.16 (5.0 \times 5.0 \mu\text{m}^2)$	~117	This work

spectroscopy, electron paramagnetic resonance, electron spin resonance, active species trapping experiments, etc. This study is expected to offer a novel and efficient strategy to promote the CMP performance of CeO₂ via constructing the CeO₂-UV-KPS polishing system.

CRediT authorship contribution statement

Yang Chen: Writing – original draft, Methodology, Conceptualization. **Pingyang Li:** Validation, Investigation. **Chao Wang:** Supervision, Project administration, Methodology. **Luning Zhong:** Software, Investigation, Data curation. **Ailian Chen:** Writing – review & editing, Supervision, Resources, Funding acquisition.

Declaration of competing interest

The authors declare that they have no known competing financial interests or personal relationships that could have appeared to influence the work reported in this paper.

Acknowledgements

The work was supported by the National Natural Science Foundation of China (Grant Nos. 52275174, 52175444, and 51875052), and the Sichuan Science and Technology Program (2021JDJQ0014).

Data availability

Data will be made available on request.

References

- [1] I. Jang, J.S.A. Carneiro, J.O. Crawford, Y.J. Cho, S. Parvin, D.A. Gonzalez-Casamachin, J. Baltrusaitis, R.P. Lively, E. Nikolla, Electrocatalysis in solid oxide fuel cells and electrolyzers, *Chem. Rev.* 124 (2024) 8233–8306.
- [2] X. Fan, D. Li, Y. Shu, Y. Feng, F. Li, Confinement effect and application in catalytic oxidation-reduction reaction of confined single-atom catalysts, *ACS Catal.* 14 (2024) 12991–13014.
- [3] S.B. Putla, M. Kamali, B. Swapna, B.M. Reddy, P. Sudarsanam, Review of shape-controlled CeO₂ nanocatalysts for purification of auto-exhaust pollutants, *ACS Appl. Nano Mater.* 7 (2024) 6749–6771.
- [4] S. Zhou, L. Wang, S. Gao, X. Chen, C. Zhang, D. Yu, X. Fan, X. Yu, Z. Zhao, Research progress on preparation of metal oxide catalysts with porous structure and their catalytic purification of diesel engine exhausts gases, *ACS Catal.* 14 (2024) 6062–6127.
- [5] C. Pei, S. Chen, D. Fu, Z.J. Zhao, J. Gong, Structured catalysts and catalytic processes: transport and reaction perspectives, *Chem. Rev.* 124 (2024) 2955–3012.
- [6] Z. Luo, Z. Zhang, F. Zhao, C. Fan, J. Feng, H. Zhou, F. Meng, X. Zhuang, J. Wang, Advanced polishing methods for atomic-scale surfaces: a review, *Mater. Today Sustain.* 27 (2024) 100841.
- [7] P.S. He, C.W. Tu, K.C. Shie, C.Y. Liu, H.Y. Tsai, D.P. Tran, C. Chen, Chemical mechanical planarization of nanotwinned copper/polyimide for low temperature hybrid bonding, *J. Electroanal. Chem.* 969 (2024) 118544.
- [8] Y.C. Fang, C.H. Lai, C.C. Li, Dispersion stabilization of carbonyl iron particles and its applications in chemical mechanical planarization, *Colloid Surface A* 683 (2024) 133003.
- [9] J. Seo, J.U. Hur, S. Kim, Y.S. Kim, Y.H. Kim, K. Bae, K. Lee, G.S. An, Recovery and reuse of magnetic silica-coated iron oxide particles for eco-friendly chemical mechanical planarization, *Colloid Surface A* 694 (2024) 134064.
- [10] X. Han, R. Liu, B. Tan, F. Wang, M. Yan, X. Zhao, J. Zhao, Research progress on the application of ceria nanoparticle as abrasives in dielectric layer CMP and post cleaning: structure, morphology, doping, and mechanism, *Colloid Surface A* 679 (2023) 132551.
- [11] J. Ma, N. Xu, J. Cheng, Y. Pu, A review on the development of ceria for chemical mechanical polishing, *Powder Technol.* 444 (2024) 119989.
- [12] A. Othman, A. Gowda, D. Andreescu, M.H. Hassan, S.V. Babu, J. Seo, S. Andreescu, Two decades of ceria nanoparticle research: structure, properties and emerging applications, *Mater. Horiz.* 11 (2024) 3213.
- [13] G. Xu, Z. Zhang, F. Meng, L. Liu, D. Liu, C. Shi, X. Cui, J. Wang, W. Wen, Atomic-scale surface of fused silica induced by chemical mechanical polishing with controlled size spherical ceria abrasives, *J. Manuf. Process.* 85 (2023) 783–792.
- [14] Y.S. Lin, K.S. Lin, W.C. Tsai, N.V. Mdiou, C.Y. Tang, U.S. Jeng, Cetyltrimethylammonium bromide reformed ceria nanocomposites of chemical mechanical planarization for silica wafers, *J. Taiwan Inst. Chem. E.* 150 (2023) 105079.
- [15] L. Wang, G. Ren, W. Xie, J. Zhang, D. Pan, S. Wang, Simple and facile synthesis of single-crystal CeO₂ abrasives and its highly efficient removal mechanism on SiO₂ film, *Appl. Surf. Sci.* 654 (2024) 159510.
- [16] G. Ren, L. Wang, S. Wang, Innovative synthesis of CeO₂ nanoparticles for advanced chemical mechanical polishing, *Colloid Surface A* 705 (2025) 135764.
- [17] C. Chen, S. Zhao, X. Li, T. Tan, W. Liao, H. You, Preparation of CeO₂ particles via ionothermal synthesis and its application to chemical mechanical polishing, *Colloid Surface A* 694 (2024) 134194.
- [18] A. Gordeev, S. Kuznetsova, E. Lyutova, O. Khalipova, D. Fedorishin, L. Selyunina, A. Malchik, Investigation of processes of obtaining cerium dioxide sol with polyvinyl alcohol having bioactive properties, *Ceram. Int.* 49 (2023) 7580–7588.
- [19] J. Li, R. He, G. Guo, Y. Li, Y. Liao, Y. Li, Synthesis of hierarchical layered quasi-triangular Ce(OH)CO₃ and its thermal conversion to ceria with high polishing performance, *ACS Omega* 8 (2023) 8519–8529.
- [20] J. Paick, S. Hong, J.Y. Bae, J.Y. Jyoung, E.S. Lee, D. Lee, Effective atomic N doping on CeO₂ nanoparticles by environmentally benign urea thermolysis and its significant effects on the scavenging of reactive oxygen radicals, *ACS Omega* 8 (2023) 22646–22655.
- [21] Y. Orita, M. Akizuki, Y. Oshima, Dual-stage method using supercritical and subcritical water for precise control of size and distribution of CeO₂ nanoparticles, *Ind. Eng. Chem. Res.* 59 (2020) 3035–3043.
- [22] L. Brugnoli, K. Miyatani, M. Akaji, S. Urata, A. Pedone, New atomistic insights on the chemical mechanical polishing of silica glass with ceria nanoparticles, *Langmuir* 39 (2023) 5527–5541.
- [23] M.D. Biase, L. Brugnoli, K. Miyatani, M. Akaji, T. Yoshida, S. Urata, A. Pedone, Impact of atomic defects on ceria surfaces on chemical mechanical polishing of silica glass surfaces, *Langmuir* 40 (2024) 6773–6785.
- [24] J. Cheng, S. Huang, Y. Li, T. Wang, L. Xie, X. Lu, RE (La, Nd and Yb) doped CeO₂ abrasive particles for chemical mechanical polishing of dielectric materials: experimental and computational analysis, *Appl. Surf. Sci.* 506 (2020) 144668.
- [25] E. Kim, J. Lee, C. Bae, H. Seok, H.U. Kim, T. Kim, Effects of trivalent lanthanide (La and Nd) doped ceria abrasives on chemical mechanical polishing, *Powder Technol.* 397 (2022) 117025–117032.
- [26] A. Chen, S. Wang, J. Pan, T. Wang, Y. Chen, Development of Zr- and Gd-doped porous ceria (pCeO₂) abrasives for achieving high-quality and high-efficiency oxide chemical mechanical polishing, *Ceram. Int.* 48 (2022) 14039–14049.
- [27] J. Ma, N. Xu, Y. Luo, Y. Lin, Y. Pu, Enhancing the polishing efficiency of CeO₂ abrasives on the SiO₂ substrates by improving the Ce³⁺ concentration on their surface, *ACS Appl. Electron. Mater.* 5 (2023) 526–536.
- [28] Z. Li, L. Jin, Z. Cao, C. Zhang, X. Cao, G. Han, S. Peng, Y. Liu, Development and characterization of a novel RE³⁺ doped core-shell CeO₂ abrasive system and its glass CMP investigations, *Appl. Surf. Sci.* 638 (2023) 158055.
- [29] X. An, J. Wang, X. Tang, W. Chen, W. Guan, C. Liu, D. Peng, Experimental study and DFT+U calculations on the impact of Rare-Earth ion (La³⁺, Sm³⁺, Y³⁺, Yb³⁺) doped CeO₂ core-shell abrasives on polishing performance, *Appl. Surf. Sci.* 676 (2024) 161028.
- [30] Y. Wu, M. Song, X. Hao, P. Mu, Q. Zhang, Kilogram-scale recovery of La/Ce and regeneration of rare-earth polishing powder products from ceria-based polishing powder waste, *ACS Sustainable Resour. Manage.* 1 (2024) 1408–1420.
- [31] Y. Fan, J. Jiao, L. Zhao, J. Tang, C. Chen, N. Fan, Nd-doped porous CeO₂ abrasives for chemical mechanical polishing of SiO₂ films, *Mat. Sci. Semicon. Proc.* 175 (2024) 108265.
- [32] Y. Chen, Y. Xia, C. Wang, J. Pan, T. Wang, A. Chen, Nanocasting synthesis of mesoporous CeO₂ particle abrasives from mesoporous SiO₂ hard templates for enhanced chemical mechanical polishing performance, *Ceram. Int.* (2024), <https://doi.org/10.1016/j.ceramint.2024.10.236>.
- [33] Z. Zhang, N. Wang, X. Wang, Z. Zhao, C. Dong, X. Tan, Y. Zheng, Z. Feng, X. Zhong, J. Yang, X. Huang, Enhanced chemical mechanical polishing (CMP) performance of porous self-assembled spherical cerium oxide via RE(La/Pr/Nd) doping, *Appl. Surf. Sci.* 679 (2025) 161236.
- [34] A. Chen, Y. Duan, Z. Mu, W. Cai, Y. Chen, Meso-silica/Erbium-doped ceria binary particles as functionalized abrasives for photochemical mechanical polishing (PCMP), *Appl. Surf. Sci.* 550 (2021) 149353.
- [35] T. Wang, Y. Chen, A. Chen, Y. Chen, Development of carbon sphere/ceria (CS/CeO₂) heterostructured particles and their applications to functional abrasives toward photochemical mechanical polishing, *Appl. Surf. Sci.* 593 (2022) 153449.
- [36] Y. Fan, J. Jiao, L. Zhao, J. Tang, Preparation of lanthanide-doped polystyrene/CeO₂ abrasives and investigation of slurry stability and photochemical mechanical polishing performance, *Colloid Surface A* 656 (2023) 130508.
- [37] Y. Chen, L. Zhong, A. Chen, M. Fu, X. Lu, Highly dispersed Gd-CeO₂ nanocrystals supported on mesoporous silica composite particles towards photochemical (photo-assisted chemical) mechanical polishing, *Ceram. Int.* 49 (2023) 16932–16943.
- [38] Z. Kou, C. Wang, W. Zhou, A. Chen, Y. Chen, Trivalent lanthanum and ytterbium doped meso-silica/ceria abrasive systems toward chemical mechanical polishing (CMP) and ultraviolet irradiation-assisted photochemical mechanical polishing (PCMP), *Appl. Surf. Sci.* 657 (2024) 159733.
- [39] N. Xu, Y. Luo, J. Ma, Y. Lin, X. Zhu, Y. Pu, Enhancement mechanism of Y-doped Ce_{1-x}Y_xO₂ for photocatalytic-assisted chemical-mechanical polishing, *Mater. Today Commun.* 38 (2024) 107791.
- [40] N. Xu, Y. Luo, Y. Lin, J. Ma, Y. Pu, The influence of CeO₂ abrasive size on the performance of photocatalytic assisted chemical-mechanical polishing by Y/Pr co-doping strategy, *Colloid Surface A* 684 (2024) 133107.
- [41] N. Xu, Y. Lin, Y. Luo, Y. Huo, K. Gao, Z. Gao, Y. Pu, Effect of surfactants with different ionizing properties on dispersion stability and PCMP properties of CeO₂ nanoparticle polishing slurry, *Ceram. Int.* (2024), <https://doi.org/10.1016/j.ceramint.2024.11.070>.

- [42] N. Yang, F. Pang, J. Ge, One-pot and general synthesis of crystalline mesoporous metal oxides nanoparticles by protective etching: potential materials for catalytic applications, *J. Mater. Chem. A* 3 (2015) 1133–1141.
- [43] C. Ma, X. Li, Q. Zhu, M. Zhang, X. Sun, Effects of Gd³⁺-doping on the fabrication and performances of highly transparent (Lu, Gd)₂O₃: Eu solid-solution ceramics, *J. Alloy Compd.* 970 (2024) 172478.
- [44] X. Xia, J. Li, C. Chen, Y. Lan, X. Mao, F. Bai, Optimal rare-earth (La, Y and Sm) doping conditions and enhanced mechanism for photocatalytic application of ceria nanorods, *Nanotechnology* 32 (2021) 195708.
- [45] P. Sharma, O. Pandey, Enhanced photocatalytic activity with metal ion doping and co-doping in CeO₂ nanoparticles, *Solid State Sci.* 126 (2022) 106846.
- [46] B. Liu, C. Li, G. Zhang, X. Yao, S. Chuang, Z. Li, Oxygen vacancy promoting dimethyl carbonate synthesis from CO₂ and methanol over Zr-doped CeO₂ nanorods, *ACS Catal.* 8 (2018) 10446–10456.
- [47] A. Liyanage, S. Perera, K. Tan, Y. Chabal, K. Balkus, Synthesis, characterization, and photocatalytic activity of Y-doped CeO₂ nanorods, *ACS Catal.* 4 (2014) 577–584.
- [48] X. Yang, Z. Xiang, J. Wu, P. He, Y. Qi, S. Chen, Y. Lu, R. Xie, Z. Liu, C. He, Research progress on the construction of oxygen vacancy defects and application in photocatalytic oxidation of elemental mercury, *Fuel* 355 (2024) 129440.
- [49] B. Safaviniya, Y. Wang, C. Jiang, C. Roman, P. Darapaneni, J. Larriviere, D. Cullen, K. Dooley, J. Dorman, Enhancing Ce_xZr_{1-x}O₂ activity for methane dry reforming using subsurface Ni dopants, *ACS Catal.* 10 (2020) 4070–4079.
- [50] M. Guo, J. Lu, Y. Wu, Y. Wang, M. Luo, UV and visible Raman studies of oxygen vacancies in rare-earth-doped ceria, *Langmuir* 27 (2011) 3872–3877.
- [51] C. Yang, Y. Lu, L. Zhang, Z. Kong, T. Yang, L. Tao, Y. Zou, S. Wang, Defect engineering on CeO₂-based catalysts for heterogeneous catalytic applications, *Small Struct.* 2 (2021) 2100058.
- [52] M.A. Mavuso, P.R. Makgwane, S.S. Ray, Heterostructured CeO₂-M (M = Co, Cu, Mn, Fe, Ni) oxide nanocatalysts for the visible-light photooxidation of pinene to aroma oxygenates, *ACS Omega* 5 (2020) 9775–9788.
- [53] P. Cop, R. Maile, Y. Sun, O. Khalid, I. Djerdj, P. Esch, S. Heiles, H. Over, B. Smarsly, Impact of aliovalent/is valent ions (Gd, Zr, Pr, and Tb) on the catalytic stability of mesoporous ceria in the HCl oxidation reaction, *ACS Appl. Nano Mater.* 3 (2020) 7406–7419.
- [54] S. Zhao, D. Kang, Y. Liu, Y. Wen, X. Xie, H. Yi, X. Tang, Spontaneous formation of asymmetric oxygen vacancies in transition-metal-doped CeO₂ nanorods with improved activity for carbonyl sulfide hydrolysis, *ACS Catal.* 10 (2020) 11739–11750.
- [55] P. Sane, S. Tambat, S. Sontakke, P. Nemade, Visible light removal of reactive dyes using CeO₂ synthesized by precipitation, *J. Environ. Chem. Eng.* 6 (2018) 4476–4489.
- [56] K. Yan, C. Wen, R. Li, B. Zhang, T. Liu, Q. Liu, Z. Zhou, Morphological optimized CeO₂ and Cu-doped CeO₂ nanocrystals for hydrogen production by solar photo-thermochemical water splitting based on surface photoinduced oxygen vacancies, *Appl. Surf. Sci.* 636 (2023) 157779.
- [57] S. Chen, L. Li, W. Hu, X. Huang, Q. Li, Y. Xu, Y. Zuo, G. Li, Anchoring high-concentration oxygen vacancies at interfaces of CeO_{2-x}/Cu toward enhanced activity for preferential CO oxidation, *ACS Appl. Mater. Interfaces* 7 (2015) 22999–23007.
- [58] Y. Li, Z. Wei, F. Gao, L. Kovarik, R.A.L. Baylon, C.H.F. Peden, Y. Wang, Effect of oxygen defects on the catalytic performance of VO_x/CeO₂ catalysts for oxidative dehydrogenation of methanol, *ACS Catal.* 5 (2015) 3006–3012.
- [59] G. Mathankumar, P. Bharathi, M. Mohan, S. Harish, M. Navaneethan, J. Archana, P. Suresh, G. Mani, P. Dhivya, S. Ponnusamy, C. Muthamizhchelvan, Synthesis and functional properties of nanostructured Gd-doped WO₃/TiO₂ composites for sensing applications, *Mater. Sci. Semicond. Process* 105 (2020) 104732.
- [60] J. Yao, Z. Yin, Z. Zou, Y. Li, Y-doped V₂O₅ With Enhanced Lithium Storage Performance, 7, *RSC Adv.* 2017, pp. 32327–32335.
- [61] M. FuentezTorres, F. OrtizChi, C. EspinosaGonzález, M. Aleman, A. CervantesUribe, J. TorresTorres, M. Kesarla, V. CollinsMartínez, S. Godavarthi, L. MartínezGómez, Facile synthesis of Zn doped g-C₃N₄ for enhanced visible light driven photocatalytic hydrogen production, *Top. Catal.* 64 (2021) 65–72.
- [62] L. Wang, P. Zhou, Y. Yan, D. Guo, Modeling the microscale contact status in chemical mechanical polishing process, *Int. J. Mech. Sci.* 230 (2022) 107559.
- [63] S. Gao, T. Li, Y. Zhang, S. Yuan, R. Kang, Insights into interfacial mechanism of CeO₂/silicon and atomic-scale removal process during chemo-mechanical grinding of silicon, *Langmuir* 39 (2023) 16606–16617.
- [64] J. Chen, L. Fang, H. Chen, K. Sun, S. Dang, J. Han, Soft abrasive facilitating materials removal of SiO₂/Si bilayer materials: a molecular dynamics study, *Mater. Chem. Phys.* 293 (2023) 126927.
- [65] S. Jiang, J. Wang, J. Lu, B. Wang, X. Li, M. Mei, Preparation and mechanical properties of core-shell PS&CeO₂ composite abrasive particles, *Langmuir* 40 (2024) 8115–8125.
- [66] Z. Ni, Q. Fan, G. Chen, M. Dai, Z. Chen, D. Bian, S. Qian, Influence of cerium oxide abrasive particle morphologies on polishing performance, *Cryst. Res. Technol.* 59 (2024) 2300308.
- [67] L.M. Cook, Chemical processes in glass polishing, *J. Non. Cryst. Solids* 120 (1990) 152–171.
- [68] J. Seo, J. Lee, J. Moon, W. Sigmund, U. Paik, Role of the surface chemistry of ceria surfaces on silicate adsorption, *ACS Appl. Mater. Interfaces* 6 (2014) 7388–7394.
- [69] G. Li, C. Xiao, S. Zhang, S. Luo, Y. Chen, Y. Wu, Study of the humidity-controlled CeO₂ fixed-abrasive chemical mechanical polishing of a single crystal silicon wafer, *Tribol. Int.* 178 (2023) 108087.
- [70] T. Onodera, H. Takahashi, S. Nomura, First-principles molecular dynamics investigation of ceria/silica sliding interface toward functional materials design for chemical mechanical polishing process, *Appl. Surf. Sci.* 530 (2020) 147259.
- [71] R. Ma, S. Zhang, T. Wen, P. Gu, L. Li, G. Zhao, F. Niu, Q. Huang, Z. Tang, X. Wang, A critical review on visible-light-response CeO₂-based photocatalysts with enhanced photooxidation of organic pollutants, *Catal. Today* 335 (2019) 20–30.
- [72] T. Montini, M. Melchionna, M. Monai, P. Fornasiero, Fundamentals and catalytic applications of CeO₂based materials, *Chem. Rev.* 116 (2016) 5987–6041.
- [73] L. Zhang, T. Wang, X. Lu, Potassium persulfate as an oxidizer in chemical mechanical polishing slurries relevant for copper interconnects with cobalt barrier layers, *J. Mater. Sci.* 55 (2020) 8992–9002.
- [74] L. Tong, Z. Li, Y. Ma, L. Zhao, Synthesis of CeO₂-loaded composite catalysts of ZIF-67 for activation of persulfate degradation of Congo red dye, *Colloid Surface A* 685 (2024) 133189.
- [75] W. Wang, S. Ye, Q. Liu, Y. Li, Y. Li, P. Wang, Ternary electrochemiluminescence biosensor based on Ce₂Sn₂O₇@MSN luminophore and Au@NiO-CeO₂ as a co-reaction accelerator for the detection of prostate specific antigen, *Microchem. J.* 205 (2024) 111258.
- [76] Y. Xu, X. Tang, Y. Xiao, H. Tang, H. Lin, Y. Lv, H. Zhang, Persulfate promoted visible photocatalytic elimination of bisphenol A by g-C₃N₄-CeO₂ S-scheme heterojunction: the dominant role of photo-induced holes, *Chemosphere* 331 (2023) 138765.
- [77] G. Feng, P. Cheng, W. Yan, M. Boronat, X. Li, J.H. Su, J. Wang, Y. Li, A. Corma, R. Xu, J. Yu, Accelerated crystallization of zeolites via hydroxyl free radicals, *Science* 351 (2016) 1188–1191.
- [78] D. Shi, W. Zhou, T. Zhao, Polishing of diamond, SiC, GaN based on the oxidation modification of hydroxyl radical: status, challenges and strategies, *Mat. Sci. Semicon. Proc.* 166 (2023) 107737.
- [79] Y. Fan, Z. Zhang, J. Yu, X. Deng, C. Shi, H. Zhou, F. Meng, J. Feng, Atomic surface of quartz glass induced by photocatalytic green chemical mechanical polishing using the developed SiO₂@TiO₂ core-shell slurry, *Nanoscale Adv* 6 (2024) 1380–1391.
- [80] R. Schmitt, A. Nenning, O. Kravins, R. Korobko, A.I. Frenkel, I. Lubomirsky, S. M. Hailef, J.L.M. Rupp, A review of defect structure and chemistry in ceria and its solid solutions, *Chem. Soc. Rev.* 49 (2020) 554–592.
- [81] K.O. Abdulwahab, M.M. Khan, J.R. Jennings, Doped ceria nanomaterials: preparation, properties, and uses, *ACS Omega* 8 (2023) 30802–30823.